

Layer-to-Layer Stability of Linear Layerwise Spatially Varying Systems: Applications in Fused Deposition Modeling

Efe C. Balta¹, *Graduate Student Member, IEEE*, Dawn M. Tilbury², *Fellow, IEEE*,
and Kira Barton¹, *Member, IEEE*

Abstract—Closed-loop control applications for additive manufacturing (AM) technologies introduce unique challenges in control-oriented modeling and controller development. There have been developments in current literature to model the temporal and spatial dynamics of AM processes. The temporal dynamics of AM processes are often modeled using tools from fluid dynamics and mechanics to represent the material deposition and the motion of the deposition system. Spatial dynamics are often modeled by representing the spreading dynamics of the deposited material in the layerwise spatial domain. An important challenge with the spatial dynamics of AM processes is to understand the performance of the layer-to-layer (L2L) spatial dynamics under spatial disturbances in the system. To this end, this article presents a linear layerwise spatially varying (LLSV) systems modeling framework to represent the L2L spatial height evolution of a generic AM process. The proposed unifying modeling framework can easily represent various AM processes. An L2L stability measure is provided as a performance measure for the spatial dynamic state of an AM process. L2L stability is a novel analysis tool to understand and analyze the spatial characteristics of AM processes. Fundamental L2L stability definitions for a nominal system model and a system model with known Gaussian spatial noise are presented. Theoretical robustness bounds for L2L stability are experimentally compared to a fused deposition modeling (FDM) process. The results show that the theoretical robustness bounds given in this work provide an important foundation for developing novel closed-loop L2L spatial control applications.

Index Terms—Fault detection, layered manufacturing, robust stability, stability, three-dimensional printing, tolerance analysis.

I. INTRODUCTION

ADDITIVE manufacturing (AM) is a prominent advanced manufacturing technology that allows for additively creating 3-D structures across a variety of length scales. In an AM process, a numerically controlled positioning system

deposits material (in a single layer) by either depositing material on a build plate (material deposition process) or transforming the material into a shaped solid form (often from powder or liquid form). After a single layer is formed, the positioning stage moves in the vertical direction (or the build platform moves vertically to accommodate a new layer) to form subsequent layers on top of the previous ones to create a 3-D geometry. AM technologies have been developed at a variety of length scales ranging from microscale to meter scale, with a diversity of material options ranging from engineered materials and polymers to metals.

An important open research area in AM is closed-loop process control [1], [2]. AM process dynamics can be analyzed in two domains. Temporal dynamics constitute the transient response of the deposition process and include material pre-process (e.g., heating), volumetric flow of material through a deposition nozzle [3]–[5], and the motion of the deposition system [6]–[8]. Spatial dynamics constitute the spatial characteristics of the process and include the change of material volume and location as a function of space, deposited material interactions with the build plate, and the geometry of the deposited material and the printed part [9]–[14]. Although most of the temporal dynamics can be modeled using existing tools in robotics, physics, and kinematics, the spatial dynamics of AM processes pose research challenges that require novel modeling and control tools. In current practice, most AM processes lack closed-loop spatial dynamical control, which results in midprocess failures and reliability issues that restrict the widespread use of AM processes. The lack of closed-loop spatial dynamical control is partly due to a lack of appropriate real-time topography feedback and also due to a lack of control-oriented models that are suitable for control applications. By developing spatial dynamical modeling methods and corresponding analysis tools, it will be possible to develop efficient closed-loop controllers for high-performance AM processes to ensure reliability and quality.

A. Motivation and Problem Statement

Spatial dynamics are crucial to ensure that an AM printed part conforms to the design specifications. Layer-to-layer (L2L) spatial dynamics entails the interaction of deposited materials at adjacent layers. Material characteristics and spatial evolution involve complex physical phenomena that have often been analyzed via numerical simulations [15]–[18].

Manuscript received August 18, 2020; accepted November 10, 2020. Date of publication January 12, 2021; date of current version October 8, 2021. Manuscript received in final form December 9, 2020. This work was supported in part by NSF under Grant 1544678 and in part by the National Institute of Standards and Technology (NIST) under Award 70NANB16H205 and Award 70NANB19H090. Recommended by Associate Editor T. Oomen. (Corresponding author: Efe C. Balta.)

The authors are with the Department of Mechanical Engineering, University of Michigan, Ann Arbor, MI 48109 USA (e-mail: baltaefe@umich.edu; tilbury@umich.edu; bartonkl@umich.edu).

Color versions of one or more figures in this article are available at <https://doi.org/10.1109/TCST.2020.3044237>.

Digital Object Identifier 10.1109/TCST.2020.3044237

However, these simulation tools are generally not suitable for closed-loop control applications. A control-oriented L2L spatial dynamical model may represent the height evolution of the AM process over a spatial discretization. By utilizing a discretized representation, it is possible to develop state-space models of the L2L spatial dynamics. Therefore, a model for control of the AM spatial dynamics should describe the L2L spatial dynamics and capture the material interactions between layers. In addition, stability properties of the spatial dynamics and a notion of L2L stability can be utilized to describe and quantify the performance of AM spatial dynamics (and subsequently an AM printed part) over the layer domain.

Therefore, to enable closed-loop L2L control of AM spatial dynamics, appropriate control-oriented models should be developed [14]. Defining the appropriate models and L2L stability measures will provide a detailed analytical framework for spatial process dynamics in high-performance AM applications and enable closed-loop control. Within this context, two problems are of interest in this work: (P1) how to develop a mathematical framework to define control-oriented models for L2L AM spatial dynamics and (P2) how to provide L2L stability measures to analyze the performance of spatial dynamics under known spatial disturbances.

The mathematical framework in this work involves spatial dynamical systems that describe AM processes, given as

$$\mathbf{g}_{k+1} = f(k, \mathbf{g}_k, \mathbf{u}_k) \quad (1)$$

where $k \in \mathbb{Z}$ is the layer index, $\mathbf{g}_k \in \mathbb{R}^n$ is the (spatial) state of the system, and $\mathbf{u}_k \in \mathbb{R}^m$ is the control input (related to the material input). Due to the explicit dependence on the layer k , the dynamics of the system may vary between the layers. As (1) describes a spatially additive process, $\{\mathbf{g}_k\}_{k=k_0}^{k_n}$ is strictly increasing and can be lower bounded by a positive-semidefinite function. In the remainder of this article, two problems are addressed: a linear layerwise spatially varying (LLSV) model for the general nonlinear system in (1) is developed to address (P1) and L2L stability properties of the L2L spatial trajectories $\{\mathbf{g}_k\}_{k=k_0}^{k_n}$ are provided to address (P2).

B. Literature Review

Computational models have been developed for the L2L spatial dynamics of AM processes [16]–[19]. While most of these models have high accuracy, the tools used for evaluating such models are computationally expensive. In addition, computational models are often very complex and do not allow for closed-form representations to build closed-loop control applications.

Control-oriented models have also been proposed to model the spatial dynamics of AM processes. In [12], liquid drop deposition and spreading dynamics for an ink-jet AM process are presented. In [10] a spatial modeling framework for electrohydrodynamic-jet printing (e-jet), a micro-AM process, is introduced and an efficient spatial iterative learning control algorithm is introduced. Drop spreading dynamics for the e-jet spatial deposition process are presented in [9], and various heightmap models for L2L dynamics at varying fidelities are

presented in [20]. A task-basis controller model to ensure uniform deposition width in a microrobotic deposition is given in [3]. Control models for the deposition height of metal AM processes are given in [11] and [21]–[24]. While controllers for AM spatial dynamics in the previous literature utilize difference or differential dynamical models of the spatial dynamics over a discretization, no unified modeling framework has been adopted. Many different models serving similar purposes are developed for various control applications. In addition, the spatial dynamic behavior of the proposed models in the presence of spatial disturbances is often not explicitly modeled. Many of the models lack the capability to express the effect of deposition path directionality on the L2L dynamics, which is essential for extrusion-based processes. For model and process uncertainties, Altin *et al.* [13] presented an interval model to account for uncertainties that arise in most practical AM applications. Nevertheless, a performance measure to characterize the spatial dynamics is not provided in the current literature. This is an important gap for the analysis of the spatial dynamics of AM processes. While variations of the well-known Lyapunov stability are provided for many AM spatial control applications [3], [6], [11], [13], [25], a similar measure for the L2L spatial dynamics to quantify the performance of a printed part has not yet been proposed.

In this work, we present an LLSV model that builds on existing models such as [10] to provide a framework that is able to represent existing spatial models and is extensible to provide control-oriented models with additional capabilities, such as uncertainty models, path directionality, various cross-sectional geometries, and spatial performance metrics for closed-loop controller designs. A spatial modeling framework specific to fused deposition modeling (FDM), where directionality of deposition path changes the spatial dynamics, is presented, and initial results on the L2L stability of FDM spatial dynamics are given in prior work [14]. Here, we formalize a novel class of LLSV systems that generalize [14] and provide the formal definitions and comprehensive analysis tools for L2L stability of LLSV systems under known spatial disturbances. Similarly, L2L stability is a novel analysis tool to characterize the spatial dynamics of L2L processes and quantify the performance of the printed part with respect to the desired physical attributes, such as optical, mechanical, or electrical properties.

C. Contributions to Literature and Article Organization

The main contributions of this work are the following:

- 1) a novel linear spatial dynamic modeling framework for AM processes and a switched affine system (SAS) representation;
- 2) formal definitions of layerwise regularity and L2L stability measures in the context of well-known Lyapunov stability, generalizing [14];
- 3) a formal analysis of robustness margins for L2L stability measures under spatial disturbances to characterize probabilistic L2L stability results;
- 4) comparison of theoretical versus experimental robustness margins with an experimental study for FDM.

The rest of this article is organized as follows. Section II provides the preliminary definitions, notations, and assumptions. Section III presents the LLSV model by introducing its constituents based on their contributions to the L2L spatial dynamics. Section IV provides the definitions of L2L stability and a theoretical framework for robustness margins in the presence of known spatial Gaussian noise in the system. Section V presents a case study on FDM and a comparison of the theoretical results to experimental data. Section VI gives concluding remarks for this article.

II. PRELIMINARIES

A. Notations Used in This Article

\mathcal{F}_E denotes a fixed inertial frame on the substrate (build plate), defined in \mathbb{R}^3 , with the orthogonal directions of unit length ($\hat{i}_E, \hat{j}_E, \hat{k}_E$). The 3-D physical vectors are denoted with boldface letters and a vector arrow, e.g., \vec{r} . Vectors are denoted with boldface letters, e.g., $\mathbf{x} \in \mathbb{R}^n$ denotes a vector in n -dimensional space. The norms $\|\cdot\|_1, \|\cdot\|_2, \|\cdot\|_\infty$ are the ℓ_1, ℓ_2 , and ℓ_∞ norms and the induced matrix norms, respectively. A sequence of vectors is denoted by $\{\mathbf{x}_i\}_{i=n_0}^{n_f}$. Letter h is reserved for functions of height, the magnitude of the equivalent physical vector in the \hat{k}_E direction. Lowercase letter k denotes the layer index throughout this article. Similarly, variables indexed with k denote layer-dependent variables. Vector \mathbf{e}_i^n denotes the unit vector for the i th dimension of an n -dimensional space (e.g., $\mathbf{e}_1^2 = [1, 0]^T$). Sets are denoted with capital letters e.g., A , with cardinality $|A|$.

Matrices are denoted with capital boldface letters, e.g., $\mathbf{A} \in \mathbb{R}^{n \times m}$. The element at the i th row and j th column of \mathbf{A} is denoted by $\mathbf{A}[i, j]$. The spectral radius of \mathbf{A} is denoted by $\rho(\mathbf{A})$. Vectorization operation is denoted with $\text{vec}(\cdot)$ and its inverse, matricization, is denoted with $\text{vec}^{-1}(\cdot, n, m)$. A function $\varphi : \mathbb{R}_{\geq 0} \rightarrow \mathbb{R}_{\geq 0}$ is a class \mathcal{K} function [26, Sec. 4.4] if it is strictly increasing, continuous, and $\varphi(0) = 0$.

B. Definitions

Definition 1 (Power-Series Bounded Matrix): A matrix $\mathbf{M} \in \mathbb{R}^{n \times n}$ is power-series bounded if $\limsup_{r \rightarrow \infty} \|\mathbf{M}^r\|_\infty = \bar{m} < \infty$ exists or equivalently if $\rho(\mathbf{M}) \leq 1$ and the eigenvalues on the unit circle are of index 1 [27].

Proposition 2 (Corollary to Gelfand's Formula): For a matrix $\mathbf{M} \in \mathbb{R}^{n \times n}$, the following property holds for $r \geq 1$, $r \in \mathbb{Z}_{>0}$:

$$\rho(\mathbf{M}) \leq \|\mathbf{M}^r\|^{1/r}.$$

Proof: This follows from [28, Proof of Corollary 5.6.14], which includes the proposition statement given here. \square

The following definitions are used to represent the physical AM process by formal mathematical notation. An AM process is defined in a finite volume in \mathbb{R}^3 , called volume of interest (VOI). The VOI is defined by a rectangular cuboid

$$\mathcal{V} = \{\mathbf{x} \in \mathbb{R}^3 \mid \mathbf{x} \in [0, i_E^{\max}] \times [0, j_E^{\max}] \times [0, k_E^{\max}]\}$$

where $(\cdot)_E^{\max}$ denotes the upper limit in each direction in \mathcal{F}_E . A layer is the material deposition on a 2-D cross section of

the VOI, with the normal of the cross section aligned with \hat{k}_E direction.

The material deposition follows a predefined path $p(k, \gamma) : \mathbb{Z}_{>0} \times [\gamma_0, \gamma_f] \rightarrow L_k$, where L_k is the 2-D deposition plane in \mathcal{V} for layer k , $\gamma \in \mathbb{R}$ is a path parameter, $p(\cdot, \gamma)$ is a Lipschitz continuous mapping, $p(k, \gamma_0)$ is the initial point, and $p(k, \gamma_f)$ is the final point of the path and $\gamma_0 < \gamma_f$.

Remark 3: In practice, the temporal execution of the deposition path of an AM process may include discontinuous jumps between deposition points in the geometry. Here, we define the predefined path $p(k, \gamma)$ to represent the spatial deposition geometry for a single layer, which may be viewed as the overall spatial representation of the deposition path. Thus, as long as the deposition path is connected, we are able to define $p(k, \gamma)$. We do not treat the cases with spatially disconnected deposition paths in this work for simplicity of presentation.

The AM process is defined as the sequential material deposition in a VOI, starting with an initial layer $k = 1$ and continuing in predefined increments in the \hat{k}_E -direction. The predefined increment between the layers is called the layer height, denoted by h_ℓ . In this work, paths of all layers k are predefined and fixed for the AM process. Furthermore, h_ℓ is uniform and fixed for all the layers in the AM process.

The dynamics of the AM process can be analyzed in two domains, as described in [14]. Two important attributes of the spatial dynamics of the AM process are the in-layer and the L2L attributes. In-layer attributes are related to the deposition of material within a single layer. L2L attributes (i.e., L2L spatial dynamics) relate the material deposition on one layer to a subsequent layer. In other words, L2L spatial dynamics describe the height evolution of the printed part across multiple layers.

C. Assumptions

In the presented spatial dynamical model, the dynamics of material flow are assumed to be well known for the duration of the process. A list of standing assumptions for this work is as follows.

- A1): Temporal dynamics of the AM process are stable and in steady state.
- A2): Material deposition within layer k follows a predefined spatial deposition path $p(k, \gamma)$ accurately (i.e., within some precision that ensures that the material is deposited at the desired spatial location) in the spatial domain, for all layers ($\forall k$).
- A3): Spatial dynamics (and consequently the spatial dynamical state) of the AM process are measurable. The spatial dynamics are measurable at the end of deposition for a layer, including any layerwise post-process (e.g., material curing, mechanical shape modification, and so on).
- A4): Spatial dynamics are observed as a result of material input in the AM process, and each layer k in the process has a predefined uniform layer height h_ℓ .

Assumption A1) ensures that the temporal dynamics are stable for the analysis of spatial dynamics in this work. Assumption A2) states that the deposition system follows a

predefined path correctly and the disturbances in the process do not alter the actual deposition path in the process. Assumptions A3) and A4) ensure that the spatial dynamics are a result of material deposition in the process. Note that we only require the spatial state to be measurable at the end of the material deposition process within a layer, including any additional layerwise process treatments that may be necessary (see [11], [13], [22], [29]). While layerwise post-processes, such as material curing, may influence the deposited spatial dynamics, we consider these influences as part of the spatial dynamics and do not consider the individual effects of material deposition versus process treatment in this work.

III. FORMULATION OF THE PROPOSED MODEL

This section provides the first contribution of this article as a formulation of the proposed LLSV model and the model representation as a SAS. The spatial dynamics of AM processes are represented on a discretization of a domain of interest. First, a discretization scheme for a given VOI is presented and a matrix representation denoting the height evolution over the discretization is given. Then, discretization of a continuously defined deposition path and the local path frame is introduced. Using the discretization scheme, the LLSV system model is introduced and a simplified reformulation of the spatial dynamics is given. An uncertainty model in the form of spatial noise is provided at the end of the section.

A. Discretization of the VOI

To define the spatial dynamic state of the AM process, it is desirable to define a suitable discretization of the VOI \mathcal{V} . We consider the layerwise deposition as always aligned with $\hat{\mathbf{k}}_E$ and define the deposition plane $L_k = \{\mathbf{x} \in \mathbb{R}^2 \mid [\mathbf{x}^T, h_k]^T \in \mathcal{V}\}$, where h_k denotes the deposition height for layer k (e.g., $h_k = kh_\ell$). Let a_i and a_j denote the discretization size in the $\hat{\mathbf{i}}_E$ - and $\hat{\mathbf{j}}_E$ -directions, respectively, shown in Fig. 1. Discretization in the $\hat{\mathbf{i}}_E$ direction is defined by the ordered set $\Lambda_i = \{x \in \mathbb{R} \mid x = a_i d, x \in [0, i_E^{\max}], d \in \mathbb{Z}_{\geq 0}\}$ and similarly defined for the $\hat{\mathbf{j}}_E$ -direction $\Lambda_j = \{x \in \mathbb{R} \mid x = a_j d, x \in [0, j_E^{\max}], d \in \mathbb{Z}_{\geq 0}\}$. Then, the discretization of the layer plane D is given as $\Lambda = \{\mathbf{x} \in L \mid \mathbf{x} \in (\Lambda_i \times \Lambda_j)\}$. Λ is assumed to be identical for all layers.

To denote the height at the spatial locations, the matrix $\mathbf{H} \in \mathbb{R}^{n_i \times n_j}$ represents the locations of spatial grid Λ , where each element $\mathbf{H}[m, n]$ corresponds to a spatial location $\lambda(m, n) = (\Lambda_i[m], \Lambda_j[n])$. A realization of the matrix \mathbf{H} at a given layer k denotes the height at the discretized locations in that layer. Overloading the notation, let $h(\mathbf{H}[i, j], k)$ denote the height of the spatial location $\mathbf{H}[i, j]$ up to layer k . Thus, the spatial height matrix $\mathbf{H}(\mathbf{H}, k) \in \mathbb{R}^{n_i \times n_j}$ with the discretization Λ for layer k is denoted with

$$\mathbf{H}(\mathbf{H}, k) = \begin{bmatrix} h(\mathbf{H}[0, 0], k) & \cdots & h(\mathbf{H}[0, n_j - 1], k) \\ \vdots & \ddots & \vdots \\ h(\mathbf{H}[n_i - 1, 0], k) & \cdots & h(\mathbf{H}[n_i - 1, n_j - 1], k) \end{bmatrix}. \quad (2)$$

Now, we can define the spatial dynamic state for layer k as

$$\mathbf{g}_k = \text{vec}(\mathbf{H}(\mathbf{H}, k)). \quad (3)$$

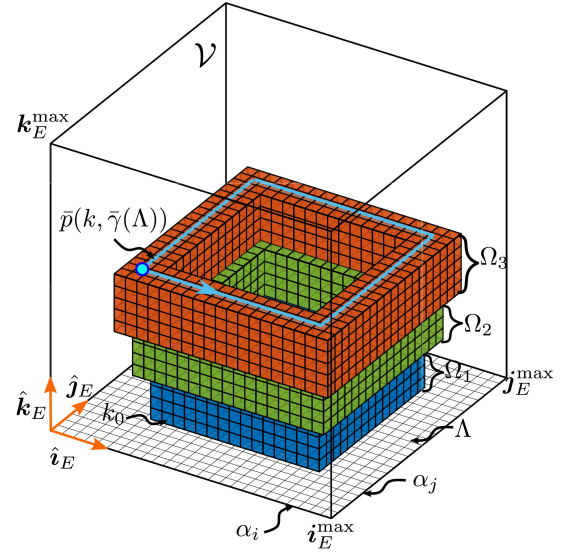


Fig. 1. Conceptual setting to describe the LLSV system as an AM process. Within the VOI \mathcal{V} , the deposition of layers starting from the initial layer k_0 over the spatial discretization λ parameterized by a_i, a_j is shown. Three-layer groups Ω_i are shown with five layers in each layer group and the deposition path $\bar{p}(k, \bar{\gamma}(\Lambda))$ for the final layer along with the deposition direction is highlighted in light blue with the start point/endpoint of the path shown with the blue filled circle. The deposition path is aligned with the grid, which results in material deposition centered on the grid points.

Using the underlying discretization Λ , it is possible to represent the spatial dynamic state as a vector $\mathbf{g}_k \in \mathbb{R}^{n_g}$, where $n_g = n_i n_j$, or as a matrix by using the $\text{vec}^{-1}(\mathbf{g}_k, n_i, n_j)$ operation. Therefore, \mathbf{g}_k represents the total height evolution (in the $\hat{\mathbf{k}}_E$ -direction) in the process up to layer k . The number $n_g \in \mathbb{Z}$ denotes the size of the discretization Λ and will be used in place of $n_i n_j$ throughout the rest of this article. The discretization Λ represents a finite number of spatial locations in D . Each spatial location can be viewed as a node of a graph, with n_g nodes in total. We define the graph $G = (\Lambda, \mathcal{E})$, with the edges \mathcal{E} in the graph connecting each spatial location $\lambda \in \Lambda$ to its neighboring spatial locations (including diagonals) within Λ . A conceptual representation of G is given in Fig. 1 as the bottom grid indicated as Λ . Each intersection in the grid represents a location $\lambda \in \Lambda$, and the grid shows the edges \mathcal{E} between the locations with the diagonal edges between locations omitted in the figure for visual simplicity. The graph G is a simple graph with self-loops, and thus, its adjacency matrix is positive semidefinite with possible nonzero diagonal entries.

B. Discretization of the Deposition Path on a Single Layer

Given the discretization Λ , discretization schemes for the deposition path and the local path frames are given here. The deposition path $p(k, \gamma)$ is continuous with respect to the parameter γ . Define $\gamma(\tau) \in [\gamma_0, \gamma_f]$ as a continuously increasing parameter along the path parameterized by the variable τ , so that $\gamma(0) = \gamma_0$ and $\gamma(f) = \gamma_f$. An instantaneous direction vector is then defined as $\bar{\mathbf{v}}_\tau = p(k, \gamma(\tau + \epsilon_p)) - p(k, \gamma(\tau))$, on the interval $\tau \in [0, f - \epsilon_p]$, for small $\epsilon_p > 0$. Similarly, the instantaneous normalized direction vector is given by $\hat{\mathbf{v}}_\tau$. While the choice of ϵ_p affects the direction that $\hat{\mathbf{v}}_\tau$ is pointing

toward, the analysis of this effect will not be presented here with the understanding that suitable ϵ_p can always be selected so that $\hat{\mathbf{v}}_\tau$ is a “tangent-like” vector. Finally, the local path frame \mathcal{F}_p is defined such that $\hat{\mathbf{k}}_p$ is aligned with $\hat{\mathbf{k}}_E$, $\hat{\mathbf{i}}_p$ is aligned with $\hat{\mathbf{v}}_\tau$, and $\hat{\mathbf{j}}_p = \hat{\mathbf{k}}_p \times \hat{\mathbf{i}}_p$ as expected, where \times denotes the vector cross product.

In practice, the deposition path is defined by a sequence of spatial locations on Λ . To do so, the discretization sizes α_i, α_j must be chosen small enough to minimize the distortion on the continuous path $p(k, \gamma)$. To represent the deposition at the discretization Λ , define the discretized sequence of points on the path as $\bar{p}(k, \bar{\gamma}(\Lambda)) \triangleq \{\lambda_m\}_{m=1}^{n_p}$, where each λ_m is called a deposition location and denotes a spatial location $\lambda(i, j) \in \Lambda$, the parameter $\bar{\gamma}(\Lambda)$ represents the discrete values of γ along the deposition path that aligns with Λ , and n_p is the number of points in the discretized deposition path. Choosing the parameter ϵ_p such that both $p(k, \gamma(\tau + \epsilon_p))$ and $p(k, \gamma(\tau))$ are aligned with Λ ensures that the local frame \mathcal{F}_p is always well-defined with respect to the discretization. For example, if $\alpha_i = \alpha_j = \hat{\alpha} \in \mathbb{R}$, choosing $\epsilon_p = \hat{\alpha}$ ensures that a deposition path without diagonal movements $\bar{p}(k, \bar{\gamma}(\Lambda))$ is aligned with Λ , as shown in Fig. 1 (light blue). We drop the dependence on the discretization and the layer index for the path whenever it is clear from the context for brevity.

Remark 4: Note that while deposition paths that are not aligned with Λ are possible by defining the proper path variables, the spatial representation may become complicated depending on the cross-sectional geometry, the discretization size α_i and α_j , and the AM process itself. For the simplicity of discussions in this work, we focus on the cases where the deposition path aligns with the spatial grid with a sufficiently fine grid size.

C. Linear Layerwise Spatially Varying Systems

To model the L2L evolution of the spatial dynamic state at the spatial discretization Λ , an LLSV model is presented in this section. LLSV is essentially a discrete linear parameter-varying (LPV) model where the state of the system (\mathbf{g}_k) is the total height up to layer k (e.g., $\mathbf{H}(\Lambda, k)$) and the parameter evolution is in terms of layer progression (e.g., k to $k+1$). The LLSV model is constructed as

$$\mathbf{g}_{k+1} = \mathbf{A}_k \mathbf{g}_k + \mathbf{B}_k \mathbf{u}_k \quad (4)$$

where \mathbf{A}_k is the spatial register matrix, \mathbf{B}_k is the input matrix, and \mathbf{u}_k is the spatial input vector. In this section, first, the spatial effect of the deposition input (\mathbf{B}_k) is modeled, and then, the effect of the previous layer (\mathbf{A}_k) is given.

1) *Effect of Material Deposition Input:* Material deposition along the path $p(k, \gamma)$ results in height evolution on each spatial location with material input. A shape function to describe the local cross-sectional height evolution as a function of distance from deposition location is defined by $c(p, \theta, r) : L_k \times \mathbb{R}^{n_\theta} \times S \rightarrow \mathbb{R}$, where p is the path mapping, $\theta \in \mathbb{R}^{n_\theta}$ is a parameter vector for a given geometry, and $r \in S \subset \mathbb{R}$ is the Euclidean distance from the deposition point in the $\hat{\mathbf{j}}_p$ direction (in the local path frame \mathcal{F}_p). Note that since $c(p, \theta, r)$ defines the height change in a finite interval,

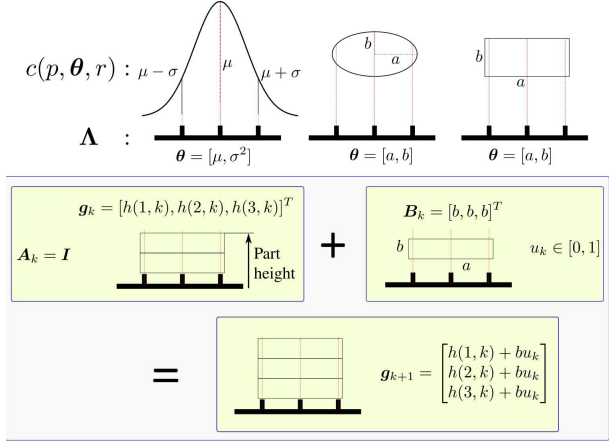


Fig. 2. Three different shape functions, their corresponding shape parameters, and their discretization on Λ (with discretization size α). These shape functions are used for characterizing the cross-sectional shape of deposited materials at each layer. A simple example of the L2L dynamics on a rectangular cross-sectional shape is shown on the bottom.

it has finite support for the compact domain S on which the cross-sectional geometry is defined, and it is zero elsewhere.

Remark 5: Definition of the shape function can be extended to 2-D height evolution for systems that have height evolution with radial symmetry, by defining the ball $S \triangleq \beta(p(k, \gamma), r) \subset \mathbb{R}^2$ as the domain.

Some examples of θ from the literature shown with their discretization in Fig. 2 are as follows.

- 1) For a Gaussian bell-curve shape, θ encodes the mean and covariance [9], [10], [12].
- 2) For an ellipsoidal shape, θ encodes the minor and major radii [14], [18], [30].
- 3) For a rectangular shape, θ encodes the height and width of the rectangle [4], [31].

While $c(p, \theta, r)$ defines a continuous shape function at the cross section of the deposition path, the analysis over the discretization Λ requires discretization of the shape function. Also, note that the shape parameters may depend on the material properties of the AM process and process-specific physical conditions.

Define $\tilde{\mathbf{c}}(\lambda_m) \in \mathbb{R}^{n_i \times n_j}$ as the discretized matrix representation of the shape function at the deposition location $\lambda_m \in \bar{p}$, for the path sequence \bar{p} defined previously. $\tilde{\mathbf{c}}(\lambda_m)$ is evaluated by sampling the function $c(p, \theta, r)$ centered at the deposition location λ_m over the discretization Λ . $\tilde{\mathbf{c}}(\lambda_m)$ can be viewed as the discretized spatial deposition impulse response of an AM process (i.e., cross section of material spread in Λ due to an impulse deposition at deposition location λ_m). Note that by defining appropriate shape functions for diagonal depositions in the discretization Λ , it is possible to extend the presented models to various deposition paths. We do not treat such cases in this work and identify them as part of future work.

Remark 6: The discrete representation of the shape function is denoted with a matrix of the size of Λ ($\tilde{\mathbf{c}}(\lambda_m)$ centered at the deposition location λ_m and the rest zero padded for full dimension) for uniform notation.

Using the discretized shape representation $\tilde{\mathbf{c}}(\lambda_m)$, define $\mathbf{c}_m = \text{vec}(\tilde{\mathbf{c}}(\lambda_m))$ as the input-to-shape response for a unit material input at the m th deposition location in $\bar{p}(k, \bar{\gamma}(\Lambda))$.

The vector $\mathbf{c}_m \in \mathbb{R}^{n_g}$ denotes the height distribution as a result of unit material input to the system. The spatial height map as a result of the unit input is denoted by the matrix $\text{vec}^{-1}(\mathbf{c}_m, n_i, n_j)$. Examples of the spatial height map representation are given in [10], [11], [13], [14], [20], and [32]. For the linear layerwise representation, define $\mathbf{B}_k \in \mathbb{R}^{n_g \times n_u}$ and $\mathbf{u}_k \in \mathbb{R}^{n_u}$, where n_u is the number of input channels (spatial locations with material input). We can take $n_u = n_p$ without loss of generality and define

$$\mathbf{B}_k = [\mathbf{c}_1, \mathbf{c}_2, \dots, \mathbf{c}_{n_u}] \quad (5)$$

$$\mathbf{u}_k = [u_1, u_2, \dots, u_{n_u}]^T \quad (6)$$

where $u_i \in [0, 1]$ is the normalized material input parameter to the AM process, which is defined as a physical input quantity such as pressure applied to the deposition system at a specific spatial location. A similarly layer-varying spatial height map model for e-jet printing is given in [20]. Note that $\mathbf{c}_i \mathbf{u}_i$ is the discretized cross-sectional shape scaled by the magnitude of the input \mathbf{u}_i and, thus, the name input-to-shape response. In this work, we utilize a linear input-to-shape response by noting that the nonlinear effects on the input dynamics may be approximated within the operating range of the input. Examples of linear input-to-shape responses include [10], [12]–[14], [22], [33], and [34]. While nonlinear and state-dependent relationships (e.g., $\mathbf{c}_i(\mathbf{g}_k)$) may outperform linear models [15], [18], [20], [29], they are not discussed here for simplicity. For control applications with L2L feedback available to the controller, an idealized shape function that is spatially invariant has been utilized in many of the works in the literature [10]–[13].

2) *Effect of the Previous Layer*: Material deposition at layer $k + 1$ is added on top of the previous layer k . Therefore, the effect of the previous layer on the height evolution of the subsequent layer must be captured in the spatial dynamics of the AM process.

A spatial register matrix $\mathbf{A}_k \in \mathbb{R}^{n_g \times n_g}$ is defined by the spatial height information relationship between different spatial locations in Λ across subsequent layers (i.e., from layer k to $k + 1$). Due to the physical interpretation of the height relationship, the information can be scaled by at most one; in other words, a scaling factor $\kappa \in [0, 1]$ can be applied to any height relationship.

Each $\mathbf{g}_k[m] \in \mathbf{g}_k$ denotes the height information of a point in Λ (i.e., height at the spatial location m up to layer k). In addition, define the mapping $M : \mathbb{Z}_{>0} \times \Lambda \rightarrow \mathbb{Z}(k, m)$, where $\mathbb{Z}(k, m) \subseteq \{1, \dots, n_g\}$, to map the height relationship between spatial locations so that each point in \mathbf{g}_k is scaled and mapped to another point in \mathbf{g}_{k+1} . This mapping is constructed based on the physical interactions of the materials deposited in subsequent layers. An example mapping is given in [14]. Formally, $M(k, m) = \{w \in \mathbb{Z}_{\geq 0} | w \in \mathbb{Z}(k, m)\}$, i.e., $M(k, m)$ is the set of locations w on layer $k + 1$ where the spatial height information is related to the height of $\mathbf{g}_k[m]$. Then, the matrix \mathbf{A}_k is constructed as the following sum over the mapping for each location in Λ :

$$\mathbf{A}_k = \sum_{m=1}^{n_g} \sum_{v \in M(k, m)} \kappa_v \mathbf{e}_v^{n_g} (\mathbf{e}_m^{n_g})^T \quad (7)$$

where $\mathbf{e}_v^{n_g}$ is the v th unit basis vector of \mathbb{R}^{n_g} and $\kappa_v \in [0, 1]$ is the scaling factor based on the AM process, height evolution geometry, and material properties. The scaling κ_v may also be state-dependent (e.g., $\kappa_v(\mathbf{g}_k)$). Note that if M is a self-mapping (i.e., $M(k, m) = \{m\}$), and $\kappa_v = 1, \forall v$, then $\mathbf{A}_k = \mathbf{I}$. As an example of self-mapping, consider AM processes that involve material curing after the deposition of a layer so that after a deposited layer is cured and solidified (see A3), its height information is additive (i.e., mapped to the next layer with $\kappa = 1$) [12], [32] (for additional L2L models with self-mapping, see [22], [33], [34]). For extrusion-based processes (see [3], [14], [29], [35]) or other deposition processes (i.e., remelting phenomenon [11]), the height information in the previous layer may be scaled in relation to the next layer. In the case study, we provide a special case for the FDM process where we constrain $\kappa_v \in [0, 1]$ to model the nonzero L2L intersection behavior of the process [14], [29]. The matrix \mathbf{A}_k may be precomputed for many processes based on the layerwise deposition path $\bar{p}(k, \bar{\gamma}(\Lambda))$ and the material interactions in the process. Fig. 2 (bottom) shows a simple example of L2L dynamics for a rectangular cross section and an identity \mathbf{A} matrix.

Based on A4), height evolution in the process is due to the material input and is bounded between the adjacent layers (e.g., $k - 1$ and k). Each row of the spatial register matrix $\mathbf{A}_k[i, \cdot]$ relates the height information from previous layer \mathbf{g}_k to the location in the subsequent layer $\mathbf{g}_{k+1}[i]$, and thus, the condition $\|\mathbf{A}_k\|_\infty \leq 1$ states that this relationship is bounded.

Remark 7: Based on the definition in (7), the following induced matrix norm relationship holds for all LLSV systems:

$$\|\mathbf{A}_k\|_1 \leq \vartheta \max_{m \in [1, n_g]} \{ |M(k, m)| \}$$

where $\vartheta \in \mathbb{R}_{\geq 0}$ is given by $\vartheta = \max\{\kappa_v\} \leq 1$.

D. SAS Reformulation

Based on Assumptions A2) and A4), \mathbf{u}_k and \mathbf{B}_k are predefined for a specific geometry and process based on the fixed deposition paths that will be deposited at a layer. The model given in (4) can be reformulated into a simpler form as an SAS with predefined switches. This representation allows for grouping similar layers together and creates a succinct formulation of the spatial dynamics with a predefined control input. In addition, if the geometry of adjacent (e.g., $k - 1$ and k) layers is identical, \mathbf{u}_{k-1} and \mathbf{u}_k are identical. In practice, an AM process typically includes multiple layers with geometries that are identical. Let the tuple (k, Ω_i) denote the layer k belonging to layer group Ω_i , where Ω_i is the set of all layers in the process that has identical inputs such that $\mathbf{u}_k = \mathbf{u}_{\bar{k}}, \forall (k, \bar{k}) \in \Omega_i$. The set of all such tuples for an AM process with n_Ω layer groups is defined as

$$\Omega = \{(k, \Omega_i) \mid k = 1, \dots, n_\ell, i \in [1, n_\Omega]\} \quad (8)$$

where each layer is mapped to one and only one layer group Ω_i . An AM process may contain multiple layer groups (see Fig. 1), so the map $\sigma(k) : k \rightarrow \Omega_i$ maps a layer k to its respective layer group for $(k, \Omega_i) \in \Omega$. A switch

occurs when $\sigma(k)$ and $\sigma(k+1)$ map the subsequent layers to different Ω_i . As a result, the LLSV spatial dynamics can be represented as

$$\mathbf{g}_{k+1} = \mathbf{A}(\sigma(k), \sigma(k-1))\mathbf{g}_k + \boldsymbol{\mu}(\sigma(k)) \quad (9)$$

where the switch of the spatial register matrix depends on the layer group of the current and previous layers (i.e., k and $k-1$). Note that if $\sigma(k-1) = \sigma(k)$, then the dependence on $\sigma(k-1)$ is redundant and may be omitted for brevity. The layer group-dependent input $\boldsymbol{\mu}(\sigma(k)) \in \mathbb{R}^{n_g}$ is defined by $\boldsymbol{\mu}(\sigma(k)) = \mathbf{B}_k \mathbf{u}_k$ for all $(k, \sigma(k)) \in \Omega$.

As many practical AM processes have layer groups (for example, task groups in [36]), the representation in (9) allows one to design controllers independently for each layer group, which may result in simpler controller formulations due to the dynamical similarities within a layer group. In such cases, the controller for each layer group would switch whenever the layer group switches, and the control design should ensure stability during the switch. In addition, using layer groups, nonconstant layer heights in the AM process may be grouped together to design individual closed-loop controllers for different layer heights.

E. Uncertainty in the LLSV Model

The AM process model has uncertainty due to material properties, discretization errors, environmental conditions, and unmodeled disturbances. In this work, the effect of uncertainty on the LLSV model is represented as a spatial noise distribution in the form of a Gaussian process (GP). A spatial noise distribution is a multivariate Gaussian distribution in which each dimension represents a spatial location $\boldsymbol{\lambda} \in \Lambda$. Based on the GP framework, it is possible to define the mean and covariance of the uncertainty on the discretization Λ . Let $\bar{\boldsymbol{\lambda}} = \text{vec}(\mathbf{\Lambda})$ denote the vector with the locations in Λ , $\mathbf{m}_{\bar{\boldsymbol{\lambda}}} \in \mathbb{R}^{n_g}$ denote the mean function, and $\boldsymbol{\Sigma}_{\bar{\boldsymbol{\lambda}}} \in \mathbb{R}^{n_g \times n_g}$ denote the covariance function for the spatial noise distribution. Then, the uncertainty as a spatial noise distribution is given by the GP $\mathbf{v}(\bar{\boldsymbol{\lambda}}) \sim \mathcal{N}(\mathbf{m}_{\bar{\boldsymbol{\lambda}}}, \boldsymbol{\Sigma}_{\bar{\boldsymbol{\lambda}}})$.

The GP is assumed to be stationary with respect to the L2L spatial dynamics, for an AM process. This means that the mean and covariance of the GP remains the same over the layer domain (and over Λ). This assumption is not restrictive since the uncertainties in the spatial dynamics are most likely to be functions of the space and, thus, invariant to the height change in the AM process.

Define $\mathcal{I}(\cdot)$ as the elementwise indicator function for nonzero elements of a matrix. Then, $\mathcal{I}(\boldsymbol{\mu}(\sigma(k))) \in \{0, 1\}^{n_g}$ is a vector with ones in the locations with material deposition for layer k and zeros elsewhere. Also, define $\mathcal{I}_k \triangleq \text{diag}(\mathcal{I}(\boldsymbol{\mu}(\sigma(k))))$ as a diagonal matrix of size $n_g \times n_g$. Then, the random vector $\mathbf{v}(\boldsymbol{\mu}(\sigma(k))) \sim \mathcal{I}_k \mathcal{N}(\mathbf{m}_{\boldsymbol{\mu}(\sigma(k))}, \boldsymbol{\Sigma}_{\boldsymbol{\mu}(\sigma(k))})$ gives the spatial noise for a specific deposition geometry with input $\boldsymbol{\mu}(\sigma(k))$. The resulting LLSV model with the uncertainty term as a spatial noise distribution is given as follows:

$$\mathbf{g}_{k+1} = \mathbf{A}(\sigma(k), \sigma(k-1))\mathbf{g}_k + \boldsymbol{\mu}(\sigma(k)) + \mathbf{v}(\boldsymbol{\mu}(\sigma(k))). \quad (10)$$

IV. L2L STABILITY

In this section, the L2L stability of the system in (9) [equivalently (4)] is investigated. In addition, robustness margins for L2L stability are given for the uncertainty reformulation of the system in (10).

A. Layerwise Regularity

In order to evaluate the L2L stability of the LLSV system, some additional measures for individual layers must be defined. A reference spatial state trajectory \mathbf{g}^d for the AM process is defined based on the design of the desired end geometry, discretization Λ , and deposition path $\bar{p}(k, \bar{y}(\Lambda))$ as $\mathbf{g}^d = \{\mathbf{g}_1^d, \dots, \mathbf{g}_{n_\ell}^d\}$, where n_ℓ denotes the total number of layers. Then, define the maximal admissible height deviation from \mathbf{g}_k^d as $\boldsymbol{\omega}_k(\mathbf{g}_k^d) \in \mathbb{R}_{\geq 0}^{n_g}$ as admissible bounds for the layerwise AM process (i.e., tolerance). Note that $\boldsymbol{\omega}_k$ (dependence on \mathbf{g}_k^d is omitted for brevity) is a layer-varying parameter so that the admissible bounds on the spatial state may be varied between the layers based on the geometry or other considerations.

Definition 8 (Layer Spatial Conformance): A layer k with the spatial dynamic state \mathbf{g}_k is layer spatial conforming if $\hat{\boldsymbol{\omega}}_k^0(\mathbf{g}_k^d) \leq \mathbf{g}_k^d - \mathbf{g}_k \leq \hat{\boldsymbol{\omega}}_k^1(\mathbf{g}_k^d)$.

Here, \leq denotes elementwise less than or equal to. Layer spatial conformance denotes if the system trajectories are within the admissible bounds. The bounds $\hat{\boldsymbol{\omega}}_k^0(\mathbf{g}_k^d)$ and $\hat{\boldsymbol{\omega}}_k^1(\mathbf{g}_k^d)$ over the discretization Λ are design variables that are determined based on the prescribed layer height h_ℓ . By prescribing $\hat{\boldsymbol{\omega}}_k^0(\mathbf{g}_k^d)$ and $\hat{\boldsymbol{\omega}}_k^1(\mathbf{g}_k^d)$ independently, nonsymmetric tolerance bounds may be prescribed. For the remainder of this article, we utilize symmetric tolerances [i.e., $\hat{\boldsymbol{\omega}}_k^0(\mathbf{g}_k^d) = -\hat{\boldsymbol{\omega}}_k^1(\mathbf{g}_k^d)$] for simplicity. The following definition describes if the trajectory $\{\mathbf{g}_k\}_{k=k_0}^{n_k}$ follows \mathbf{g}^d within the admissible bounds.

Definition 9 (Layer-Wise Regularity [14]): An AM process is said to be layerwise ω -regular at layer k if $\|\mathbf{g}_k^d - \mathbf{g}_k\|_2 \leq \omega$.

Layerwise regularity states that the spatial trajectories of the LLSV system are within a tube of radius ω around \mathbf{g}^d . The numerical value of ω may be defined based on specific design considerations for part functionality (e.g., mechanical, electrical, or optical properties). A detailed discussion on the design of ω is beyond the scope of this work and not discussed here. An example of ω for dimensional performance is provided in the case study. Using the definitions of spatial conformance and layerwise regularity, L2L stability definitions are given next.

B. L2L Stability Definitions

An important property of an AM process is its geometric stability. This is the ability of subsequent layers to be built on top of the existing layers. Define $\tilde{\mathbf{g}}_k = \mathcal{I}_{k-1} \mathbf{g}_k$ as a vector with height information of the spatial locations with height change on layer k , defined by $\boldsymbol{\mu}_{k-1}$, and zeros elsewhere. The vector $\tilde{\mathbf{g}}_k$ denotes the height of the locations in Λ that had deposition for the current layer.

Definition 10 (L2L Geometric Stability [14]): An LLSV system is said to be L2L geometrically stable (L2LGS) if $\|\mathbf{g}_{k-1}\|_\infty < \min_j \{\|\tilde{\mathbf{g}}_k[j]\| > 0\}$, for all $k \in (1, n_\ell)$.

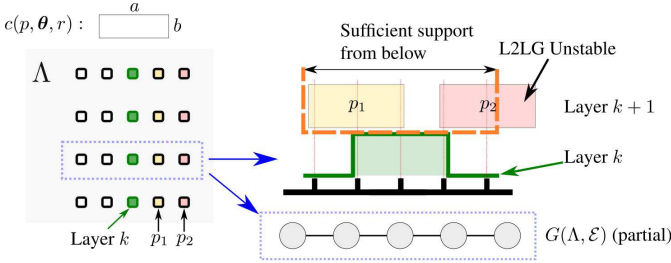


Fig. 3. Left: top view of the deposition process with a rectangular shape function. The green path labeled with Layer k is the currently deposited layer. The deposition path p_1 at layer $k+1$ is sufficiently supported from below, whereas p_2 at layer $k+1$ is not sufficiently supported from below. Right: cross-sectional view of the deposition process at layers k and $k+1$ illustrates the sufficient support condition for example. The partial graph G of the process is given below to illustrate the adjacency between the spatial locations within the dotted rectangle in Λ .

The operator $\min_j \{|\tilde{g}_k[j]| > 0\}$ denotes the magnitude of the minimum nonzero element in the vector \tilde{g}_k , with element-wise absolute value operator $|\cdot|$. Therefore, in an L2LGS system, the minimum height at the spatial locations with deposition for layer k is greater than the maximum height in layer $k-1$. Intuitively, the L2LGS condition ensures that the current spatial state \mathbf{g}_k is always “above” the preceding layer, providing a natural condition for geometrical stability of the printed part.

Remark 11: The LLSV system with A2) is L2LGS by design since the layer geometries and path planning for the AM process follow this stability condition to create reference trajectories $p(k, \gamma)$ for all $k \in (1, n_\ell]$, which in turn defines \mathbf{g}^d . Without loss of generality, the L2LGS condition holds for all LLSV systems analyzed in this work.

Going back to the graph G interpretation of the discretization Λ , any spatial state \mathbf{g}_k denotes the height on the nodes of G up to layer k . The L2L geometric stability condition requires the material deposition at the subsequent layer ($k+1$) to be sufficiently supported from below (at layer k). Sufficient support is the least amount of material present at a certain location $\lambda(m, n) \in \Lambda$ in layer k so that the deposition on the subsequent layer $k+1$ is L2LGS according to Definition 10. Sufficient support depends on the specific AM technology, geometry, and material properties. A brief analysis of the L2L geometrical stability and its implications on the input design is given in [14].

Consider the L2L dynamics shown in Fig. 3. Let \mathbf{J}_k define the adjacency matrix of the graph G and the shape function of the process be a rectangular one. We may associate the region of sufficient support in Fig. 3 with the adjacency of the graph G . In the given case, material deposited in layer k at a location λ supports the material deposition on the spatial locations immediately adjacent to it at layer $k+1$. Note that the adjacency relationship is a function of the discretization size, shape function, and the physical properties of the material and process. Therefore, the deposition on layer k in the figure provides sufficient support for the deposition path p_1 on layer $k+1$, but the path p_2 becomes L2L geometrically unstable. Based on Remark 11, we assume that the sufficient support condition holds for all LLSV systems analyzed in this work.

The L2L stability of an LLSV system is then defined based on the definitions of regularity and stability.

Definition 12 (L2L Stability): An LLSV system that is L2LGS is said to be:

- 1) L2L stable (L2LS) if for any given $\delta_c > 0$, $\exists \delta_s > 0$, such that $\|\mathbf{g}_{k_0}^d - \mathbf{g}_{k_0}\| < \delta_s$ implies $\|\mathbf{g}_k^d - \mathbf{g}_k\| < \delta_c$ for all $k \in [k_0, n_\ell]$;
- 2) L2L finite stable (L2LFS) if it is L2L stable and $\exists \xi \in (0, 1)$ such that $\|\mathbf{g}_{k+1}^d - \mathbf{g}_{k+1}\| \leq \xi \|\mathbf{g}_k^d - \mathbf{g}_k\|$ for all $k \in [k_0, n_\ell - 1]$.

Note that L2LFS denotes finite convergence of the spatial trajectories to the desired state trajectories (within a predefined precision) with a convergence rate of at most ξ . The actual ξ for a practical system determines whether perfect tracking is feasible within finitely many layers in the AM process.

While L2LS defines a stability measure for the process, we are often interested in understanding if the spatial dynamics are L2L stable with respect to the layerwise ω -regularity.

Definition 13 (L2L ω -Stability): An LLSV system that is L2L stable is said to be L2L ω -regular stable if given $\delta_c = \omega > 0$, there exists a $\delta_s \in (0, \omega)$ so that all the spatial trajectories are layerwise ω -regular.

Therefore, L2L stability of the spatial trajectories is a performance measure for the LLSV system to have geometric stability and stay close to a desired spatial trajectory \mathbf{g}^d , whereas L2L ω -regular stability implies that we can prescribe how “close” the system trajectory is to the desired trajectory.

Remark 14: Note that L2L ω -regular stability implies that L2LS can be ensured for a desired stability bound $\omega > 0$ for all layers and thus is more stringent than the nominal L2LS. Characterizing the conditions under which an LLSV system is L2LS and L2L ω -regular stable is left for future work.

Another important aspect is the relationship between the L2L stability and the stability of the error dynamics of the system, highlighted in the following remark.

Remark 15: While L2LS provides a framework to characterize the system performance, it is not readily compatible with the usual stability analysis tools as L2LS is defined with respect to the desired trajectory rather than an equilibrium for the unforced system. Therefore, by defining the error dynamics of the LLSV system with respect to a desired spatial trajectory, we utilize the transformed system dynamics to draw parallels between the L2L stability framework and the well-known Lyapunov stability.

Without loss of generality, consider the error dynamics of (9) for a single Ω_i , which we assume to be power-series bounded for the simplicity of discussion. Define the error state $\boldsymbol{\eta}_k = \mathbf{g}_k^d - \mathbf{g}_k$ and the dynamics of the error as $\boldsymbol{\eta}_{k+1} = \mathbf{A}\boldsymbol{\eta}_k$, where we use the shorthand \mathbf{A} for \mathbf{A}_k , $k \in \Omega_i$. The following lemma is given as the main result for L2L geometrical stability of an LLSV system.

Lemma 16: An LLSV system without noise, given in (9), with the error state as $\boldsymbol{\eta}_k = \mathbf{g}_k^d - \mathbf{g}_k$ is L2LGS if and only if there exists $c_0, c_1 > 0$ such that

$$\begin{bmatrix} I & (1-c_0)I \\ -c_1I & (1-c_1)I \end{bmatrix} \begin{bmatrix} \boldsymbol{\eta}_{k+1} - \boldsymbol{\eta}_k \\ \mathbf{g}_{k+1} - \mathbf{g}_k \end{bmatrix} \geq 0 \quad \forall k \in [1, n_\ell - 1].$$

Proof: Define $\boldsymbol{\pi}_1 = \bar{\mathbf{g}}_k^d - c_0 \bar{\mathbf{g}}_k$ and $\boldsymbol{\pi}_2 = \bar{\mathbf{g}}_k - c_1 \bar{\mathbf{g}}_k^d$, where $\bar{\mathbf{g}}_k^d := \mathbf{g}_k^d - \mathbf{g}_{k-1}^d$ and $\bar{\mathbf{g}}_k := \mathbf{g}_k - \mathbf{g}_{k-1}$. Then, decompose $\boldsymbol{\pi}_i = \boldsymbol{\pi}_i^+ - \boldsymbol{\pi}_i^-$, $i = 1, 2$, where $\boldsymbol{\pi}_i^+ = \max\{0, \boldsymbol{\pi}_i\}$ and $\boldsymbol{\pi}_i^- = \max\{0, -\boldsymbol{\pi}_i\}$ with the elementwise max operator. Let $c_0 = m(\bar{\mathbf{g}}_k^d) / \|\bar{\mathbf{g}}_k\|_1$, where $m(\cdot)$ denotes the smallest nonzero element of a vector. Similarly, let $c_1 = m(\bar{\mathbf{g}}_k) / \|\bar{\mathbf{g}}_k^d\|_1$.

Now, observe that with the chosen scaling factors c_0 and c_1 , nonzero elements of $\boldsymbol{\pi}_1^+$ denote the spatial locations at layer k that either has desired deposition or voids (deposition is desired, but there is none). The nonzero elements of $\boldsymbol{\pi}_1^-$ denote the spatial locations with extra deposition (deposition is not desired at these locations). Similarly, nonzero elements of $\boldsymbol{\pi}_2^+$ denote the desired and extra depositions, and nonzero elements of $\boldsymbol{\pi}_2^-$ denote voids.

L2LGS dictates that deposition at a layer must be exactly at the desired locations that are prescribed by the L2LGS reference \mathbf{g}_k^d for each k . Thus, a necessary condition for L2LGS is $\|\boldsymbol{\pi}_1^-\| + \|\boldsymbol{\pi}_2^-\| = 0$, which is possible only if $\boldsymbol{\pi}_1^- = \boldsymbol{\pi}_2^- = \mathbf{0}$. In that case, we have $\boldsymbol{\pi}_i = \boldsymbol{\pi}_i^+ \geq 0$ that results in $\bar{\mathbf{g}}_k^d - c_0 \bar{\mathbf{g}}_k = \boldsymbol{\pi}_1^+ \geq 0$, which is equivalently $\boldsymbol{\eta}_{k+1} - \boldsymbol{\eta}_k + (1 - c_0) \mathbf{I} \bar{\mathbf{g}}_k \geq 0$. Similarly, we derive $-c_1 \mathbf{I} (\boldsymbol{\eta}_{k+1} - \boldsymbol{\eta}_k) + (1 - c_1) \mathbf{I} \bar{\mathbf{g}}_k \geq 0$. Combining the last two inequalities gives the desired result.

To show the reverse direction, suppose there exists an L2LGS $\bar{\mathbf{g}}_k$ with voids. Then, it must be that $\bar{\mathbf{g}}_k - c_1 \bar{\mathbf{g}}_k^d = \boldsymbol{\pi}_2 \geq 0$. Due to the void, there exists at least one direction j in the vector $\bar{\mathbf{g}}_k$ which is zero, but is nonzero in $\bar{\mathbf{g}}_k^d$. This means that there exists no $c_1 > 0$ that can make $\bar{\mathbf{g}}_k[j] - c_1 \bar{\mathbf{g}}_k^d[j] \geq 0$, and therefore, $\boldsymbol{\pi}_2^- \neq 0$, which results in a contradiction with $\boldsymbol{\pi}_1^- = \boldsymbol{\pi}_2^- = \mathbf{0}$. A similar analysis follows for extra depositions but is omitted here for brevity, which concludes the proof. \square

Then, a formal relationship between the stability of the error dynamics and the L2L stability is given as follows.

Lemma 17: The equilibrium point $\boldsymbol{\eta}_k = \mathbf{0}$ at layer k for an LLSV system given in (4) with the error state $\boldsymbol{\eta}_k = \mathbf{g}_k^d - \mathbf{g}_k$ satisfying Lemma 16 is said to be:

- 1) L2L stable if and only if the equilibrium $\boldsymbol{\eta}_k = \mathbf{0}$ is stable in the sense of Lyapunov [26], meaning that for a given $\delta_c > 0$, $\exists \delta_s > 0$ such that $\|\boldsymbol{\eta}_{k_0}\| < \delta_s \implies \|\boldsymbol{\eta}_k\| < \delta_c, \forall k > k_0$.
- 2) L2L ω -regular stable if for $\delta_c = \omega$, $\exists \delta_s \in (0, \omega)$, with ω as the layerwise regularity bound $\forall k$.
- 3) L2LFS if and only if it is linearly convergent to zero, i.e., $\exists \zeta \in (0, 1)$ such that $\|\boldsymbol{\eta}_{k+1}\| \leq \zeta \|\boldsymbol{\eta}_k\|$.
- 4) Asymptotically stable, meaning that the equilibrium is Lyapunov stable and $\{\|\boldsymbol{\eta}_k\|\}_{k=k_0}^\infty \rightarrow 0$ as $k \rightarrow \infty$, if it is L2LFS.

Proof: The proof follows immediately from combining Lemma 16 with Definition 12. \square

Note that the equilibrium $\boldsymbol{\eta}_k = \mathbf{0}$ at layer k implies that $\mathbf{g}_k = \mathbf{g}_k^d$. Given the monotone increasing nature of the desired spatial states \mathbf{g}_k^d , the equilibrium $\boldsymbol{\eta}_k = \mathbf{0}$ is not an unforced equilibrium since the absence of an input at layer k (e.g., $\mathbf{u}_k = \mathbf{0}$) implies $\mathbf{g}_{k+1} - \mathbf{g}_{k+1}^d = \boldsymbol{\eta}_k \neq \mathbf{0}$. Therefore, the L2L stability and equilibrium stability notions are considered under the prescribed inputs to the system instead of the usual Lyapunov stability of an unforced system.

Recall that LLSV systems are strictly increasing due to the physical AM process that has additive spatial input at each layer. This property can be denoted as $\varphi_1(\|\mathbf{g}_{k_0}\|) \leq \{\|\mathbf{g}_k\|\}_{k=k_0}^{n_\ell}$, where $\varphi_1 \in \mathcal{K}$.

The findings in this section are summarized in the following.

Theorem 18: For an LLSV system in (4) with the error state $\boldsymbol{\eta}_k = \mathbf{g}_k^d - \mathbf{g}_k$ satisfying Lemma 16, the following are equivalent.

- 1) The LLSV system is L2L stable.
- 2) The equilibrium $\boldsymbol{\eta}_k = \mathbf{0}$ is stable in the sense of Lyapunov.

In addition, the following are equivalent among each other.

- 1) The LLSV system is L2L finite stable.
- 2) The sequence $\{\|\boldsymbol{\eta}_k\|\}_{k=k_0}^\infty$ is linearly convergent to zero.

Proofs for Theorem 4 were provided throughout the section.

C. Robustness to Uncertainty

The main theorems of this work are given in this section. The robustness-to-L2L stability measures presented in this section serve as analysis tools to analyze if a given LLSV system will be L2L unstable in future layers.

To define the robustness of the L2L stability bound under the uncertainties in the model given in 10, the following lemma is needed.

Lemma 19: The expected value of $\|\mathbf{v}(\boldsymbol{\mu}(\sigma(k)))\|_2$ is upper bounded by the following relationship:

$$\mathbb{E}\{\|\mathbf{v}(\boldsymbol{\mu}(\sigma(k)))\|_2\} \leq (\mathbf{tr}(\boldsymbol{\Sigma}_{\sigma(k)} + \mathbf{m}_{\sigma(k)} \mathbf{m}_{\sigma(k)}^T))^{1/2}.$$

Proof: Noting that the vector $\mathbf{v}(\boldsymbol{\mu}(\sigma(k)))$ consists of random variables from the distribution $\mathcal{N}(\mathbf{m}_{\sigma(k)}, \boldsymbol{\Sigma}_{\sigma(k)})$, the expectation of the quadratic form of $\mathbf{z} \triangleq \mathbf{v}(\boldsymbol{\mu}(\sigma(k)))$ is $\mathbb{E}\{\mathbf{z}^T \mathbf{z}\} = \mathbf{tr}(\mathbb{E}\{\mathbf{z} \mathbf{z}^T\})$. Then, the expectation is

$$\begin{aligned} \mathbb{E}\{\|\mathbf{z}\|_2\} &= \mathbb{E}\{(\|\mathbf{z}\|_2^2)^{1/2}\} \leq (\mathbb{E}\{\|\mathbf{z}\|_2^2\})^{1/2} \\ &= (\mathbf{tr}(\mathbf{v}(\mathbf{z}) + \mathbb{E}\{\mathbf{z}\} \mathbb{E}\{\mathbf{z}\}^T))^{1/2} \\ &= (\mathbf{tr}(\mathbf{v}(\mathbf{z}) + \mathbf{m} \mathbf{m}^T))^{1/2} \end{aligned}$$

with $\mathbf{v}(\cdot)$ denoting the variance matrix, which uses Jensen's inequality and the fact that square root is a concave function to derive the required result. \square

Lemma 20: For the induced norm of the register matrix of an LLSV system, the following inequality holds for some $\vartheta' \in (0, 1]$:

$$\|\mathbf{A}_k\|_2 \leq \sqrt{\vartheta' \max_{m \in [1, n_g]} \{M(k, m)\}} \quad \forall k \in [1, n_\ell].$$

Proof: The proof follows immediately by applying Hölder's inequality with the conditions given in Remark 7, $M(k, m)$ defined in Section III-C2, and $\vartheta' = (\max\{\kappa_v\} \|\mathbf{A}\|_\infty)^{-1}$. \square

Theorem 21: In a single-layer group with $\sigma(k') \rightarrow \Omega_i, \forall k' \in [k_0, k_f]$ that is $\tilde{\omega}$ -regular at layer k_0 and the state register matrix $\tilde{\mathbf{A}} \triangleq \mathbf{A}(\sigma(k), \sigma(k-1))$ defined over the range of layers k' , the LLSV system in (10) is L2L $\tilde{\omega}$ -regular stable at layer k_f in expectation if $\forall \zeta \in [1, k_f - k_0]$, we have

$$\|\tilde{\mathbf{A}}^\zeta\|_2 \|\boldsymbol{\eta}_{k_0}\|_2 + (\mathbf{tr}(\boldsymbol{\Sigma}' + \mathbf{m}' \mathbf{m}'^T))^{1/2} \leq \tilde{\omega}$$

where $\Sigma' = \Sigma_{\sigma(k)} + \tilde{A}\Sigma_{\sigma(k)}\tilde{A}^T + \dots + \tilde{A}^{\zeta-1}\Sigma_{\sigma(k)}(\tilde{A}^{\zeta-1})^T$, $\mathbf{m}' = P_{\zeta-1}(\tilde{A})\mathbf{m}_{\sigma(k)}$, $P_{\zeta-1}(\tilde{A})$ is a matrix polynomial up to power $\zeta - 1$, and $\tilde{\omega} > 0$ is the L2L stability bound (δ_c). Furthermore, if $\mathbf{m}_{\sigma(k)} = \mathbf{0}$, then

$$\|\tilde{A}^{\zeta}\|_2\|\boldsymbol{\eta}_{k_0}\|_2 + \|\mathbf{L}\|_F \leq \tilde{\omega} \quad (11)$$

where $\mathbf{L}\mathbf{L}^T = \Sigma'$.

Proof: The proof is given for $\zeta = k_f - k_0$ since the same analysis follows $\forall \zeta \in [1, k_f - k_0]$. Define $\tilde{\mathbf{v}} \triangleq \mathbf{v}(\boldsymbol{\mu}(\sigma(k)))$. The error dynamics of the LLSV system are given by

$$\boldsymbol{\eta}_{k_f} = \tilde{A}^{k_f-k_0}\boldsymbol{\eta}_{k_0} + \sum_{i=k_0}^{k_f-1}\tilde{A}^{k_f-i-1}\tilde{\mathbf{v}}.$$

The sum in this equation is a matrix polynomial up to degree $\zeta - 1$ given as

$$\sum_{i=k_0}^{k_f-1}\tilde{A}^{k_f-i-1}\tilde{\mathbf{v}} = \mathbf{I}\tilde{\mathbf{v}} + \tilde{A}\tilde{\mathbf{v}} + \dots + \tilde{A}^{\zeta-1}\tilde{\mathbf{v}}$$

which has the expected value $\mathbb{E}\{\sum_{i=k_0}^{k_f-1}\tilde{A}^{k_f-i-1}\tilde{\mathbf{v}}\} = \mathbf{m}' = P_{\zeta-1}(\tilde{A})\mathbf{m}_{\sigma(k)}$, where $P_n(\mathbf{A}) = \mathbf{I} + \mathbf{A} + \dots + \mathbf{A}^n$, and covariance $\Sigma' = \Sigma_{\sigma(k)} + \tilde{A}\Sigma_{\sigma(k)}\tilde{A}^T + \dots + \tilde{A}^{\zeta-1}\Sigma_{\sigma(k)}(\tilde{A}^{\zeta-1})^T$. Therefore, we have $\sum_{i=k_0}^{k_f-1}\tilde{A}^{k_f-i-1}\tilde{\mathbf{v}} \sim \mathcal{N}(\mathbf{m}', \Sigma')$. Taking ℓ_2 norms of both sides and their expectations yield the following inequalities:

$$\begin{aligned} \|\boldsymbol{\eta}_{k_f}\|_2 &\leq \|\tilde{A}^{k_f-k_0}\|_2\|\boldsymbol{\eta}_{k_0}\|_2 + \left\|\sum_{i=k_0}^{k_f-1}\tilde{A}^{k_f-i-1}\tilde{\mathbf{v}}\right\|_2 \\ \mathbb{E}\{\|\boldsymbol{\eta}_{k_f}\|_2\} &\leq \|\tilde{A}^{\zeta}\|_2\|\boldsymbol{\eta}_{k_0}\|_2 + (\text{tr}(\Sigma' + \mathbf{m}'\mathbf{m}'^T))^{1/2}. \end{aligned}$$

Since this defines an upper bound on the error after ζ layers, if this bound is greater than $\tilde{\omega}$, L2L $\tilde{\omega}$ -regular stability cannot be guaranteed and thus the given bound. Therefore, if the bound in the theorem holds for all layers in the analysis (i.e., $\forall \zeta \in [1, k_f - k_0]$), the system is L2L $\tilde{\omega}$ -regular stable at layer k_f , in expectation. This relationship concludes the proof of the first part. Now, suppose that $\mathbf{m}_{\sigma(k)} = \mathbf{0}$ and $\Sigma' = \mathbf{L}\mathbf{L}^T$ (this decomposition always exists since $\Sigma' \succeq \mathbf{0}$), and then

$$\begin{aligned} \mathbb{E}\{\|\boldsymbol{\eta}_{k_f}\|_2\} &\leq \|\tilde{A}^{\zeta}\|_2\|\boldsymbol{\eta}_{k_0}\|_2 + (\text{tr}(\mathbf{L}\mathbf{L}^T))^{1/2} \\ &\leq \|\tilde{A}^{\zeta}\|_2\|\boldsymbol{\eta}_{k_0}\|_2 + \|\mathbf{L}\|_F \end{aligned}$$

which concludes the proof. \square

Based on the magnitude of ζ , the bound on the error in the LLSV system is affected by the uncertainty in the system, while the effect of the initial error norm is decreasing with the increasing horizon. Using Lemma 20, the value of $\|\tilde{A}^{\zeta}\|_2$ can be approximated. Note that if $\|\tilde{A}\|_2 < 1$, we can analyze $\zeta = k_f - k_0$ (instead of $[1, k_f - k_0]$) in Theorem 21 without loss of generality (since $\|\tilde{A}\|_{\infty} < 1$). The analysis for the case where the spatial register matrix is power-series convergent is given next.

Corollary 22: If, in addition to Theorem 21, we have $\rho(\tilde{A}) < 1$ and $\varsigma = \|\tilde{A}\|_2 < 1$, then for large enough ζ and invertible $(\mathbf{I} - \tilde{A})$, the error dynamics $\boldsymbol{\eta}_k$ of the LLSV system are bounded in expectation by

$$\begin{aligned} \mathbb{E}\{\|\boldsymbol{\eta}_{k_f}\|_2\} &\leq (\text{tr}(\Sigma') + \|\mathbf{m}''\|_2^2)^{1/2} \\ &\leq (\text{tr}(\Sigma') + \varsigma'\|\mathbf{m}_{\sigma(k)}\|_2^2)^{1/2} \end{aligned}$$

where $\varsigma' = (1 - \varsigma)^{-1}$, Σ' as previously given, and $\mathbf{m}'' = (\mathbf{I} - \tilde{A})^{-1}\mathbf{m}_{\sigma(k)}$.

Proof: If $\rho(\tilde{A}) < 1$ and $\varsigma = \|\tilde{A}\|_2 < 1$, then there exists $c > 0$ where $\tilde{A}^c \simeq \mathbf{0}$ and thus $\varsigma^c \simeq 0$. By choosing $\zeta \geq c$ (assuming that this is feasible in the physical process), the sum $P_{\zeta-1}(\tilde{A})$ is equal to $(\mathbf{I} - \tilde{A})^{-1}$, and $\|\tilde{A}^{\zeta}\|_2 = 0$. The second upper bound follows from the geometric sum of the ς and the fact that $\|\tilde{A}^{\zeta}\| \leq \|\tilde{A}\|_{\infty}^{\zeta}$. \square

In addition, the following corollary to Theorem 21 provides a probabilistic bound for estimating the L2LS of an LLSV system of the form (10):

Corollary 23: For the system given in Theorem 21, if the covariance matrix has the form $\Sigma' = \sigma_s^2\mathbf{I}$, probability for the ℓ_2 -norm squared of error dynamics ($\|\boldsymbol{\eta}_{k_f}\|_2^2$) being $\tilde{\omega}^2$ -regular at layer k_f is given by

$$\mathbb{P}(\|\boldsymbol{\eta}_{k_f}\|_2^2 \leq \tilde{\omega}^2) = \mathbb{P}(\Gamma \leq \tilde{\omega}^2/\sigma_s^2)$$

where $\Gamma \sim \mathcal{X}_{n_g}^2(\psi)$ is a random variable from an n_g degrees of freedom noncentral chi-squared distribution with the noncentrality parameter $\psi = \sigma_s^{-2}\sum_{j=1}^{n_g}(\mathbf{m}^*[j])^2$ and $\mathbf{m}^* = \tilde{A}^{\zeta}\boldsymbol{\eta}_{k_0} + \mathbf{m}'$, $\zeta = k_f - k_0$.

Proof: Following the proof of Theorem 21, the error at layer k has the multivariate normal distribution $\boldsymbol{\eta}_k \sim \mathcal{N}(\tilde{A}^{\zeta}\boldsymbol{\eta}_{k_0} + \mathbf{m}', \Sigma')$. The ℓ_2 -norm squared of a random variable from this multivariate normal distribution is distributed as a noncentral chi-squared distribution with n_g degrees of freedom. For the covariance matrix of the form $\Sigma' = \sigma_s^2\mathbf{I}$, the noncentrality parameter of the distribution is given by $\psi = \sigma_s^{-2}\sum_{j=1}^{n_g}(\mathbf{m}^*[j])^2$. Therefore, the probability of the ℓ_2 -norm squared value of the error being within the stability bound squared $\tilde{\omega}^2$ is given by the cumulative distribution function of $\mathcal{X}_{n_g}^2(\psi)$. \square

Theorem 21 is stated for a single-layer group and it is a known fact that a switched system with stable subsystems may become unstable under certain switching conditions [37]. To circumvent this issue and ensure the stability of the LLSV system for all Ω_i , the following observations are given. The trajectory of the error dynamics given by $\boldsymbol{\eta}_{k+1} = \mathbf{A}_k\boldsymbol{\eta}_k$ is bounded under arbitrary switching if the joint spectral radius [38] of all $\mathbf{A}(\sigma(k), \sigma(k-1))$ in the LLSV system is power-series bounded, and the system is L2LGS. However, this is a much stronger condition than what we need in practice since the dynamics undergo a known switching sequence rather than arbitrary switching. Therefore, the stability of the switches may be analyzed off-line. Further conditions for finite convergence of the switched dynamics is given in [39, pp. 170–173].

V. CASE STUDIES ON FDM

This section presents case studies for an FDM process modeled as an LLSV system. Definitions of L2L stability and details of the LLSV model for a specific geometry are given. Leveraging the models and the experimental setup, theoretical developments on the L2L stability in the earlier sections are compared against the experimental measurement. A schematic of an FDM process is shown in Fig. 4. FDM is an AM process in which a thermoplastic material is extruded through a heated

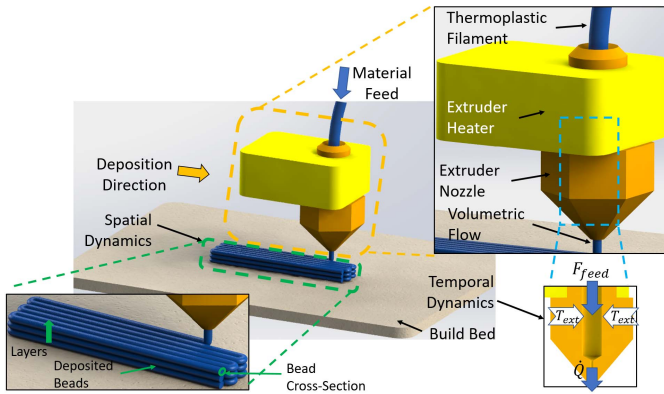


Fig. 4. Description of FDM [14]. F_{feed} is the material feed force for the extrusion process in the nozzle. T_{ext} is the heat supplied by the extruder heater. \dot{Q} is the volumetric flow through the nozzle.

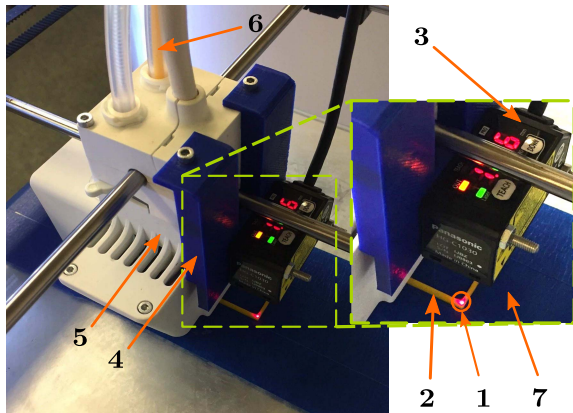


Fig. 5. Experimental setup. 1: laser measurement point. 2: square shell build geometry. 3: laser distance measurement sensor. 4: mounting piece for the sensor. 5: extruder head of the FDM printer. 6: PLA filament used in the experiment. 7: heated build plate with the painter's tape to mitigate glare.

nozzle in a numerically controlled deposition system. After a layer of material is deposited, either the deposition system or the build platform changes its height to accommodate the next deposition layer until all the layers of a 3-D object are deposited (refer to [35] and references therein for a survey of the FDM process).

This case study aims to demonstrate the practical use of the LLSV model and the L2L stability concepts presented in this work as a measure of dimensional performance. An experimental setup is used to measure the spatial state of an FDM with induced spatial noise. The theoretical bounds derived in Theorem 21 are compared to experimental results.

A. Experimental Setup

The experimental setup is shown in Fig. 5. To enable a spatial height measurement between layers, a Panasonic HG-C1030 laser point distance measurement sensor is mounted on the extruder of an Ultimaker 3 FDM printer. The laser has a 50- μm spot diameter and a 10- μm repeatability. An Arduino Mega connected to MATLAB on a Windows 10

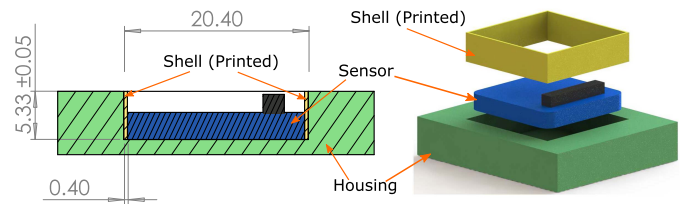


Fig. 6. Technical drawing of the assembly of the square shell geometry (left) and the exploded view of the assembly (right). The conceptual sensor that fits inside the shell and the housing. A cross-sectional view is shown in the figure and the assembly is symmetric about the axis of the cross-sectional cut.

TABLE I
EXPERIMENTAL PARAMETERS FOR THE CASE STUDY

Variable	Value
Material	PLA @ 220°C
Build bed	Glass @ 60°C
Feedrate	20mm/sec
Shell width	20.4mm
Shell height	5.33 ± 0.05mm
Layer height	$h_\ell = 0.27\text{mm}$
Design discretization	$\alpha_i = \alpha_j = 0.16\text{mm}$
Grid size	$n_i = n_j = 128$
Number of layers	$n_\ell = 20$
L2L intersection	$\bar{d} = 30.6\mu\text{m}$
Experimental discretization	$\bar{\alpha}_i = \bar{\alpha}_j = 0.2\text{mm}$
Experimental grid	$\bar{n}_i = \bar{n}_j = 103$
Extrusion per unit length	$p_e = 0.0025\text{mm}$

machine with i7-4700 CPU is used for collecting the sensor measurements at a rate of 480 Hz.

For the case study, a square shell geometry (1 bead thickness) is additively manufactured using FDM. The geometry of the shell and its assembly is shown in Fig. 6. A manufacturing scenario in which the shell geometry needs to fit inside a square slot of 20.4 mm and depth of 5.33 mm is considered with the given dimensional tolerances shown in Fig. 6. Based on these dimensional specifications, layerwise regularity and L2L ω -regular stability limits are evaluated in Section V-B. The experimental parameters for the case study are given in Table I. By ensuring L2L ω -regular stability, we can ensure that the FDM printed shell will conform to the design specifications and deliver the desired performance in terms of dimensional accuracy. Similarly, we will conclude that L2L ω -regular unstable parts will not conform to the design specifications and thus will be scrap. Thus, we utilize L2LS as an *in situ* tool for analyzing printed part performance in this case study, which is a novel approach to understand the printed part performance in AM.

B. LLSV Systems for FDM

The spatial deposition path $p(k, \gamma)$ for the square shell geometry is identical for all layers $\forall k$. Consequently, there is only a single-layer group $\sigma(k) = \Omega_1$, $\forall k \in [1, n_\ell]$. In FDM, deposited beads of subsequent layers form an intersection where they partially bond to create a sound structure [35]. As a

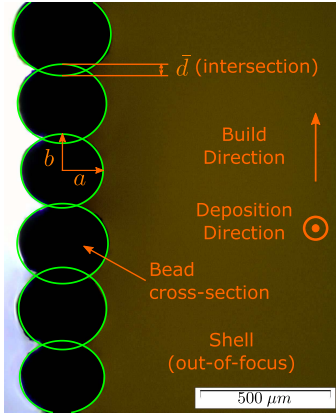


Fig. 7. Cross-sectional cutout of one of the deposited square shell specimen under a microscope. Green ellipsoids are fit to the cross sections to study the bead intersection between the subsequent layers.

result, the height evolution of the build between subsequent layers is less than the spatial input to the system, which results in a $\kappa_v < 1$ [in (7)]. In addition, due to inconsistencies (caused by transient dynamics of the fluid flow) in the material flow at the beginning of the process and the interaction of the material with the build plate, the initial layer height is observed to be less than expected during the experiments.

1) *Spatial Register Matrix for FDM*: To understand the effect of height intersection, *ex situ* measurements are performed on the printed parts. Experiment specimens cut across the cross section are measured using a microscope (see Fig. 7). Green ellipsoids are fit to each cross section in the image and their intersection amount is calculated. In practice, FDM deposition is adjusted such that the extruder nozzle presses onto the deposited material in a layer [29]. In this case study, the deposition height is adjusted to have a gap between the nozzle tip and the deposited bead to better understand the effect of spatial noise on the size of a deposited bead. Through this study, the mean value of L2L intersection between the beads of successive layers is found to be $\bar{d} = 30.6 \mu\text{m}$.

Using the laser distance measurement sensor, the profile of the surface of a printed part with 180 layers is measured and no significant change in the intersection amount is observed. As a result, the intersection amount is modeled as a constant amount across layers. The scaling factor κ_v in (7) is given as

$$\kappa_v(\mathbf{g}_k[m]) = (1 - \bar{d}/\mathbf{g}_k[m]).$$

Since $\bar{d} \ll \mathbf{g}_k, \forall k$, the value of $\kappa_v(\mathbf{g}_k)$ is strictly less than one (e.g., $\kappa_v(\mathbf{g}_k) \in (0, 1)$).

The height information at spatial locations $\lambda(1, m)$, $m \in [2, 125]$ in layer k are mapped to $\lambda(1, m)$ and the neighboring spatial locations at $\lambda(0, m)$ and $\lambda(2, m)$ in layer $k + 1$. The spatial deposition points on the corners have their height information mapped to their surrounding points. The mapping $M(k, m)$ is created by utilizing the relationship given in the above examples for all the deposition points in the process for all layers

$$\mathbf{A}(\sigma(k), \mathbf{g}_k) = \sum_{m=0}^{n_g-1} \sum_{v \in M(k, m)} \left(1 - \frac{\bar{d}}{\mathbf{g}_k[m]}\right) \mathbf{e}_v^{n_g} (\mathbf{e}_m^{n_g})^T. \quad (12)$$

Since $\kappa_v(\mathbf{g}_k) \in (0, 1)$, it is straightforward to show that $\|\mathbf{A}(\sigma(k), \mathbf{g}_k)\|_\infty < 1$ and $\rho(\mathbf{A}(\sigma(k), \mathbf{g}_k)) < 1$. Furthermore, the spectral radius $\rho(\mathbf{A}(\sigma(k), \mathbf{g}_k)), k \in [1, n_\ell]$ is upper bounded by $\kappa_v(\mathbf{g}_{n_\ell}) < 1$ for the last layer n_ℓ since the spatial state trajectory is nondecreasing.

Details of model creation to represent a bead cross section at three locations in Λ are provided in Appendix A. For simplicity of analysis, we consider the deposited bead cross sections only along the spatial locations on the deposition path $p(k, \bar{\gamma}(\Lambda))$. We employ the mapping $M(k, m) = \{m\}$ with $\kappa_v(\mathbf{g}_k) \in (0, 1)$ described as above so that $\mathbf{A}(\sigma(k), \mathbf{g}_k) = (1 - \bar{d}/\mathbf{g}_k)\mathbf{I}$, where the division is elementwise.

2) *The Effect of Noise*: To illustrate the L2L stability concept, known spatial disturbances are induced on the deposition process and the results are experimentally measured. A quadratic positive semidefinite spatial noise function is used in the case study. The function is given as

$$\mathbf{v}(\mathbf{x}, \mu) = \mu/v^2(\mathbf{x}_1^2 + \mathbf{x}_2^2) \quad (13)$$

where $v \in \mathbb{R}$ is a scale correction factor (e.g., for a spatial area of $20 \text{ mm} \times 20 \text{ mm}$ around the origin, $v = 10$) and $\mathbf{x} \in \mathbb{R}^2$ is the spatial variable and μ is the amplitude of the noise function. As the spatial location of the deposition moves away from the center of the build plate, increased noise is expected due to errors in the flatness of the build plate.

The induced noise is added as a disturbance to the extrusion command (i.e., adding noise terms to the E -axis references) in the G-Code for the FDM machine. Due to the online computational capacity available in the FDM machine, the design discretization of 0.16 mm is downsampled 1.25 times so that $\bar{a}_i = \bar{a}_j = 0.2 \text{ mm}$. As a result, the discretization used for G-Code generation has $\bar{n}_i = \bar{n}_j = 103$. The G-Code discretization is denoted by $\bar{\Lambda}$, and the deposition path is denoted by $\bar{p}(k, \bar{\gamma}(\bar{\Lambda}))$, with the vector \bar{p} as the vector with locations of deposition. Note that $\text{diag}(\mathcal{I}_k) = \mathcal{I}(\sigma(k)) = \bar{p}, \forall k$.

The spatial noise over the deposition path is given by the distribution $\mathcal{N}(\mathbf{v}'(\mathbf{x}, \mu), \sigma_e^2 \mathbf{I})$ where $\mathbf{v}'(\mathbf{x}, \mu) = \mathbf{v}(\bar{p}(k, \bar{\gamma}(\bar{\Lambda})) - \bar{\lambda}(52, 52), \mu)$, $\mathbf{x}_{(\cdot)} \in \bar{\Lambda}$, and $\bar{\lambda}(52, 52)$ is picked as the center of the square deposition discretization in $\bar{\Lambda}$. The spatial noise is then given as

$$\mathbf{v}(\mu) \sim \mathcal{I}_k \mathcal{N}(\mathbf{v}'(\mathbf{x}, \mu), \sigma_e^2 \mathbf{I}) \quad \forall k \in [1, n_\ell]. \quad (14)$$

A standard deviation of $\sigma_e = 6.62 \times 10^{-4} \text{ mm}$ is applied to all of the points, which corresponds to 0.25 of the unit filament extrusion length ($[p_e = 0.0025 \text{ mm}$ between each point in $\bar{p}(k, \bar{\gamma}(\bar{\Lambda}))$]).

The input to the system is defined as $\mathbf{u}_k = \mathcal{I}_k \mathbf{0.0025}$. The spatial noise $\mathbf{v}(\mu)$ is added to the input. To derive a linear model for the expected effect of induced Gaussian noise, a first-order approximation of the nonlinear input dynamics around the nominal layer height is derived as a function of the noise amplitude variable μ as $\bar{b}(\mathbf{u}_k + \mathbb{E}\{\mathbf{v}(\mu)\})|_{\mathbf{u}_k=p_e} \simeq 0.267 + 1.0962\mu$ with a fit residual corresponding to less than $2.5 \mu\text{m}$. Using the linear approximation, the LLSV dynamics are

$$\mathbf{g}_k = \mathbf{A}(\sigma(k), \mathbf{g}_k) \mathbf{g}_k + \mathcal{I}_k (\mathbf{0.267} + \mathbf{1.0962} \mathbf{v}(\mu)). \quad (15)$$

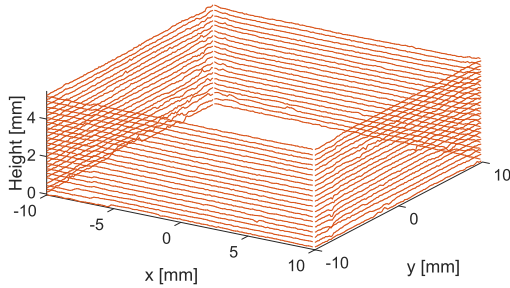


Fig. 8. Measurement data for one of the nominal prints over $\bar{\Lambda}$. At each layer, the deposition starts from the point (10, 10) and follows the corners (-10, 10), (-10, -10), and (10, -10).

Without loss of generality, we employ a \mathbf{B} matrix for the noise input as $\mathbf{B} = \mathcal{I}_k 1.0962 \mathbf{I}$ and denote the transformed input noise as $\bar{\mathbf{v}}(\mu) \sim \mathcal{N}(\mathbf{B}\mathbf{v}'(\mathbf{x}, \mu), \mathbf{B}\sigma_c^2 \mathbf{I}\mathbf{B}^T)$.

3) *Definition of L2L Stability Bounds:* Based on the dimensional tolerances shown in Fig. 6, the upper and lower deviation limits of 0.05 mm for the printed design are given. To ensure that the printed part fits within the tolerances, L2L stability bounds are chosen as $\hat{\omega}_k = \mathbf{0.05}, \forall k \in [1, n_\ell]$, and $\tilde{\omega} = \|\mathbf{0.05}\|_2$ for the layerwise regularity conditions and to ensure L2L ω -regular stability for all layers in the process (when δ_c in Definition 12 is chosen as $\tilde{\omega}$).

4) *Experimental Procedure:* Layer height for layers $k \in [1, n_\ell]$ is identically prescribed as $h_\ell = 0.27$ mm. A set of experiments is conducted for the deposition process without any induced spatial noise on the system. Then, experiments with induced spatial noise are conducted [dynamics as in (15)]. The value of μ is varied between $1.5p_e$ and $3.9p_e$ in $0.2p_e$ increments for a total of 13 levels of μ . For each spatial noise function, four experiments are conducted and *in situ* measurements of all the deposited layers are performed with the experimental setup. The bead-center heights are measured by centering the laser sensor on the deposited beads and scanning along the deposition path in the experiments. A total of 57 parts are printed for the experiments and data for a total of 1140 layers are collected. It is important to note that there is no closed-loop control implemented for any of the experiments as it is beyond the scope of the presented work.

C. Results

1) *Nominal Case Without Induced Noise:* Experimental height measurement data for one of the nominal parts over the discretization $\bar{\Lambda}$ are shown in Fig. 8. At each layer, the deposition starts from the point (10, 10) and follows the corners (-10, 10), (-10, -10), and (10, -10). The mean layer height of the seven nominal experiments is taken as the desired layer height profile \mathbf{g}^d . The mean height residuals between the desired height profile and four of the nominal prints are shown in Fig. 9. The measurements for the nominal case have an average (for each layer over seven experiments) standard deviation of 0.0175 mm. Note that this value is the statistical standard deviation and does not reflect the actual resolution of the measurement system (10 μm). The desired height profile \mathbf{g}^d is defined as the mean of nominal trajectories to mitigate the effect of inherent disturbances and noise in the experimental process.

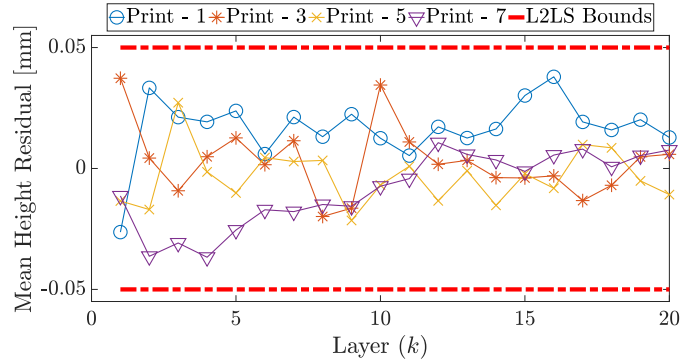


Fig. 9. Residual of the mean layer height for nominal deposition case without induced spatial noise. Mean values from four nominal prints are shown all 20 layers in the deposition process. The L2L ω -regular stability bounds for the experiment are shown with red dashed lines.

2) *Experimental Results With Induced Noise:* Experimental results for seven different spatial noise functions are given in Fig. 10. Four parts are printed for each spatial noise corresponding to different values of μ . The mean layer height for each of the layers is compared to the desired height profile defined by the nominal case to evaluate the mean height residuals. One standard deviation of the mean values from the four printed parts of each μ value is shown with the filled colors around the mean values. The L2L stability bounds are shown with red dashed lines in Fig. 10. The results presented in Fig. 10 show that the L2L stability bound is violated between the noise levels $\mu = 2.1p_e$ and $\mu = 2.3p_e$ and closer to $\mu = 2.3p_e$, which corresponds to $\mu^{\text{exp}} = 0.0057$ mm. We use the approximate value of $\mu^{\text{exp}} \approx 2.25p_e$ for further discussions.

3) *Outlook for Control Synthesis:* Here, the results in Theorem 21 are compared to the experimental bound given above to validate the theoretical framework proposed in this work. For the discretization $\bar{\Lambda}$, $\bar{p}(k, \bar{\gamma}(\bar{\Lambda}))$ has a total of 400 deposition points per layer. By construction in Section V-B1, we have $\rho(\mathbf{A}(\sigma(k), \mathbf{g}_k)) < 1$ (taken as 0.99 for analysis) and $\tilde{\omega} = \|\mathbf{0.05}\|_2 = 1$. The spatial dynamics of the deposition process are only considered at the measurement points along the $\bar{p}(k, \gamma, \bar{\Lambda})$. It is straightforward to show that the system is L2LGS as the spatial trajectories are building on top of one another to build a sound structure.

Suppose that we want to synthesize a controller to ensure L2L ω -regular stability for the remainder of the process at layer $k_0 = 1, \zeta = 19$. For an initial error η_{k_0} upper bounded by 0.015 mm (i.e., $\eta_{k_0} \leq \mathbf{0.015}$), Theorem 21 is satisfied for noise levels $\mu \in (0, 0.0014 \text{ mm}]$ with a probability of 0.97 according to Corollary 23. In comparison to the experimental bound $\mu^{\text{exp}} = 0.0057$ mm, the theoretical bound $\mu^{\text{thr}} = 0.0014$ mm is a conservative underapproximation of the actual robustness bound. This means that a controller that stabilizes the AM process according to the theoretical bounds given in Theorem 21, albeit being conservative, would indeed L2L stabilize the AM process under disturbances (with the indicated probability). This is an important finding that has not been previously presented in the literature and forms a basis for the theory of L2L stability for LLSV systems.

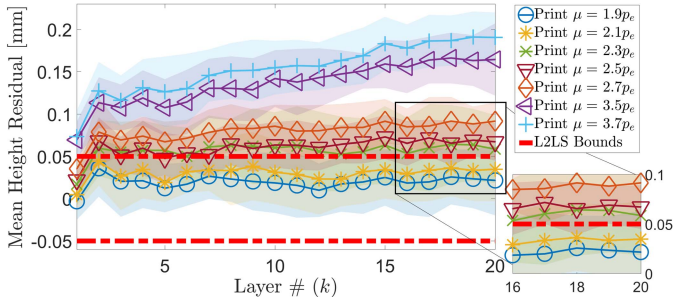


Fig. 10. Plots of the mean height residuals and their one standard deviation for four different noise values. The L2L ω -regular stability bounds for the experiment are shown with red dashed lines.

In future work, a closed-loop L2L spatial controller may utilize Theorem 21 to ensure the L2L stability of the system in a receding horizon fashion.

The gap between the noise levels for the predicted bound and the experimental bound is 0.0043 mm, which is below the measurement resolution in the experimental procedure. The discrepancy between the theoretical and experimental value is also due to the upper approximations in the formulation, which represents the worst case effect of the noise on the system and the uncertainties in the formulation of the spatial register matrix and the resolution of the first-order approximation for the effect of input.

4) *Outlook for Decision-Making*: Here, we provide additional insights on how the theoretical findings in this work (i.e., Theorem 21) can be utilized as a decision-making mechanism for an autonomous FDM process. Since L2L ω -regular unstable parts will not conform to the design specifications, it may be desirable to stop the FDM process once we predict that the resulting part will become scrap. After the current layer k_0 is measured, we utilize a binary classifier based on Theorem 21 to predict whether the process will be L2L ω -regular stable in ζ layers, in expectation. While the bound μ^{thr} is given for a projection of 19 layers, adjusting the horizon length ζ results in a more accurate prediction of the experimental robustness bounds. For a controller that stops the AM process as the prediction of L2L ω -regular instability (utilizing the LLSV model) is above a certain confidence level, adjusting the value of ζ would characterize the accuracy of the decision. To illustrate this concept, we present a receiver operating characteristic (ROC) curve for a binary classifier that predicts the L2L ω -regular instability in ζ layers using Theorem 21.

Fig. 11 shows the ROC curve for predicting whether the process will be L2L ω -regular unstable, parameterized by ζ . We have the same analysis setup with $\eta_1 \leq 0.015$ and $\tilde{\omega} = \|\mathbf{0.05}\|_2$. To evaluate the true positive and false-positive rates, we utilize the experimental data with 13 noise levels, out of which nine are L2L unstable. We utilize the classifier to predict L2L ω -regular instability and plot the results for the values of $\zeta \in [1, 19]$. We observe that a value of $\zeta = 5$ provides a true positive rate of 1 with a low false-positive rate (0.25). Similarly, a value of $\zeta = 4$ provides a false-positive rate of 0 with a high true positive rate (0.89). Thus, a decision-maker

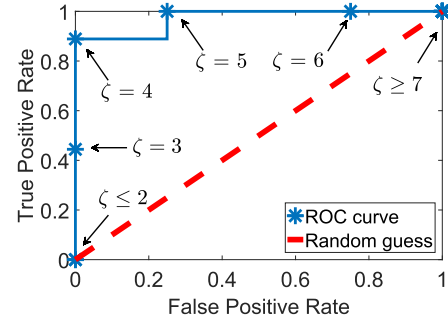


Fig. 11. ROC curve for the decision-maker utilizing a classifier based on Theorem 21 to predict whether the FDM process measured at layer $k = 1$ will be L2L ω -regular unstable. The curve is parameterized by the horizon $\zeta \in [1, 19]$ for the remaining layers in the process.

should be operated at one of these levels based on the desired operating characteristics. This result also confirms the overconservative nature of the theorem as high values of ζ cause the classifier to predict that the process will go unstable. A perfect process model would be able to completely identify L2L ω -regular stable processes from unstable ones. Based on the LLSV model derived for a specific process, the ROC curve can be experimentally constructed and implemented for a practical decision-maker. A closed-loop controller may utilize the ROC curve to tune the prediction horizon of a controller on the spatial dynamics to ensure L2L stability of the printed device for all layers, which in turn would provide guarantees on the part functionality.

The fact that theoretical developments are more accurate with shorter horizons can be explained by the accuracy of the first-order approximation around the operating point. In addition, since the spatial register matrix used here is also an approximation, the accuracy of the projections deteriorate for long-horizon lengths. By evaluating higher fidelity models of the AM processes, high-accuracy decision-makers for longer prediction horizons (ζ) may be developed.

VI. CONCLUSION

LLSV models provide a general framework for modeling the spatial dynamics of AM processes where the L2L height evolution of an AM process is modeled over a discretization of interest. In this work, a modeling and L2L stability framework for LLSV systems are proposed. Also, a theoretical bound for robustness-to-L2L stability is given and the provided bound is compared with experimental results. This theoretical framework provides a new analysis tool for the performance of the L2L spatial dynamics of AM processes. For the experimental validation, the proposed modeling framework is demonstrated on an FDM machine and an LLSV model of the process is developed. The theoretical robustness bound for L2L stability gives a conservative approximation of the actual stability bound. Therefore, L2L stability and the robustness bounds proposed in this work may be leveraged for control development of LLSV systems.

This work presents crucial findings on the stability of the spatial dynamics through the notion of L2L stability. Stronger stability conditions, such as L2L finite stability, can be used for

designing controllers that guarantee monotonic stability of the spatial dynamics over the layer domain. The initial proofs and analyses given here can be leveraged in developing closed-loop controllers for high-performance AM applications to improve process quality and reliability. Building on the modeling framework given here, linear and nonlinear spatial models of various AM processes may be developed. Alternate representations of the proposed models in the frequency domain may be developed for applications with large spatial domains. While the presented work focuses on the L2L height evolution of the spatial dynamics, the framework is flexible enough to model additional spatial properties, such as electrical or mechanical properties of the printed parts. Investigation of such applications to control part functionality is subject for future work.

APPENDIX A SHAPE FUNCTIONS AND KERNEL BASES FOR FDM BEAD MODELING

1) *Shape Function and Input for FDM*: An ellipsoid shape function with the major (a) and minor (b) radii and $\theta = [a, b]$ is chosen for the FDM process. The shape function for the FDM process is given by

$$c(p, \theta, b, y') = \frac{1}{2b} \left[\sqrt{b^2 \left(1 - \frac{\Delta y}{a^2}\right)} + b \right] \quad (16)$$

where $y' \in [y - a, y + a]$ and $\Delta y = \|y - y'\|_2^2$ is the Euclidean distance squared from a deposition point $y \in p$ in the \hat{j}_p direction, and the function is zero everywhere else.

Single-bead width is measured as 0.36 mm on average with caliper measurements. The square deposition path on Λ is given by the following spatial deposition points:

$$\begin{aligned} \bar{p}(k, \bar{\gamma}(\Lambda)) = \{ & \lambda(1, 1), \dots, \lambda(1, 126) \\ & \lambda(2, 126), \dots, \lambda(126, 126) \\ & \lambda(126, 125), \dots, \lambda(126, 1) \\ & \lambda(125, 1), \dots, \lambda(2, 1) \}. \end{aligned} \quad (17)$$

Define $\mathbf{P} \in \mathbb{R}^{n_i \times n_j}$ with ones for the spatial locations in Λ with deposition, defined by $\bar{p}(k, \bar{\gamma}(\Lambda))$ and zeros elsewhere, and define $\mathbf{p} = \text{vec}(\mathbf{P})$.

2) *Kernel Bases for Deposition Bead Modeling*: The concept of kernel basis matrices is introduced in [14] to evaluate \bar{c}_i with the correct spatial location and orientation. A kernel basis matrix has the nonzero entries that correspond to the discretized heights of the shape function at a specific orientation (e.g., $0, \pi/2$) based on the deposition path. Leveraging the adjacency and the square shape of the deposition path, the following 3×3 kernel basis matrices are given. The shorthand $c(y') = c(p, \theta, b, y')$ is used for notational brevity

$$\mathbf{K}_1 = \begin{bmatrix} 0 & 0 & 0 \\ c(y + \alpha_i) & c(y) & c(y - \alpha_i) \\ 0 & 0 & 0 \end{bmatrix}$$

$$\mathbf{K}_2 = \begin{bmatrix} 0 & c(y - \alpha_j) & 0 \\ 0 & c(y) & 0 \\ 0 & c(y + \alpha_j) & 0 \end{bmatrix} \quad \mathbf{K}_3 = \begin{bmatrix} 0 & 0 & 0 \\ 0 & c(y) & 0 \\ 0 & 0 & 0 \end{bmatrix}.$$

Since $\alpha_i = \alpha_j$ and the bead function is symmetric, $\mathbf{K}_1 = \mathbf{K}_2^T$ in this example. To understand the effect of corner overflow in the case study, the deposited parts are observed under a microscope. As a result, \mathbf{K}_3 represents the corners of the square shell.

The $\bar{c}(s_m)$ matrices for spatial inputs are evaluated in the following way for each deposition point.

- 1) For a point p on the deposition path \bar{p} , a corresponding kernel basis matrix \mathbf{K}_i is determined.
- 2) Taking the center entry of \mathbf{K}_i as the spatial location corresponding to p in Λ , the matrix is padded with zeros to have the appropriate dimensions $\mathbb{R}^{n_i \times n_j}$.

Using the $\bar{c}(s_m)$ matrices, input matrix \mathbf{B}_k is evaluated as given in (5). For the spatial locations with multiple overlapping \mathbf{K}_i matrices, a saturation function is utilized to ensure that the control input is appropriately applied to the spatial dynamics. A similar approach is presented in [14].

REFERENCES

- [1] J. Pellegrino, T. Makila, S. Mcqueen, and E. Taylor, "Measurement science roadmap for polymer-based additive manufacturing," *NIST Adv. Manuf. Ser.*, vol. 100, 2016. [Online]. Available: <https://nvlpubs.nist.gov/nistpubs/ams/NIST.AMS.100-5.pdf>
- [2] K. Barton, D. A. Bristow, D. Hoelzle, and S. Mishra, "Mechatronics advances for the next generation of AM process control," *Elsevier Mechatron.*, vol. 64, Dec. 2019, Art. no. 102281, doi: 10.1016/j.mechatronics.2019.102281.
- [3] D. J. Hoelzle, A. G. Alleyne, and A. J. W. Johnson, "Basis task approach to iterative learning control with applications to micro-robotic deposition," *IEEE Trans. Control Syst. Technol.*, vol. 19, no. 5, pp. 1138–1148, Sep. 2011.
- [4] Y. Cheng and M. A. Jafari, "Vision-based online process control in manufacturing applications," *IEEE Trans. Autom. Sci. Eng.*, vol. 5, no. 1, pp. 140–153, Jan. 2008.
- [5] I. A. Spiegel, P. Sammons, and K. Barton, "Hybrid modeling of electrohydrodynamic jet printing," *IEEE Trans. Control Syst. Technol.*, vol. 28, no. 6, pp. 2322–2335, Nov. 2020.
- [6] K. L. Barton and A. G. Alleyne, "A cross-coupled iterative learning control design for precision motion control," *IEEE Trans. Control Syst. Technol.*, vol. 16, no. 6, pp. 1218–1231, Nov. 2008.
- [7] M. Duan, D. Yoon, and C. E. Okwudire, "A limited-preview filtered B-spline approach to tracking control—With application to vibration-induced error compensation of a 3D printer," *Mechatronics*, vol. 56, pp. 287–296, Dec. 2018.
- [8] D. S. Ertay, A. Yuen, and Y. Altintas, "Synchronized material deposition rate control with path velocity on fused filament fabrication machines," *Additive Manuf.*, vol. 19, pp. 205–213, Jan. 2018.
- [9] C. P. Pannier, M. Diagne, I. A. Spiegel, D. J. Hoelzle, and K. Barton, "A dynamical model of drop spreading in electrohydrodynamic jet printing," *J. Manuf. Sci. Eng.*, vol. 139, no. 11, Nov. 2017, Art. no. 111008.
- [10] D. J. Hoelzle and K. L. Barton, "On spatial iterative learning control via 2-D convolution: Stability analysis and computational efficiency," *IEEE Trans. Control Syst. Technol.*, vol. 24, no. 4, pp. 1504–1512, Jul. 2016.
- [11] P. M. Sammons, M. L. Gegel, D. A. Bristow, and R. G. Landers, "Repetitive process control of additive manufacturing with application to laser metal deposition," *IEEE Trans. Control Syst. Technol.*, vol. 27, no. 2, pp. 566–575, Mar. 2019.
- [12] Y. Guo, J. Peters, T. Oomen, and S. Mishra, "Control-oriented models for ink-jet 3D printing," *Mechatronics*, vol. 56, pp. 211–219, Dec. 2018.
- [13] B. Altin, Z. Wang, D. J. Hoelzle, and K. Barton, "Robust monotonically convergent spatial iterative learning control: Interval systems analysis via discrete Fourier transform," *IEEE Trans. Control Syst. Technol.*, vol. 27, no. 6, pp. 2470–2483, Nov. 2019.
- [14] E. C. Balta, D. M. Tilbury, and K. Barton, "Control-oriented modeling and layer-to-layer stability for fused deposition modeling: A kernel basis approach," in *Proc. Amer. Control Conf. (ACC)*, Jul. 2019, pp. 4727–4733.
- [15] G. L. Knapp *et al.*, "Building blocks for a digital twin of additive manufacturing," *Acta Mater.*, vol. 135, pp. 390–399, Aug. 2017.

- [16] T. DebRoy, W. Zhang, J. Turner, and S. S. Babu, "Building digital twins of 3D printing machines," *Scripta Mater.*, vol. 135, pp. 119–124, Jul. 2017, doi: [10.1016/j.scriptamat.2016.12.005](https://doi.org/10.1016/j.scriptamat.2016.12.005).
- [17] H. Xia, J. Lu, and G. Tryggvason, "Fully resolved numerical simulations of fused deposition modeling. Part II—Solidification, residual stresses and modeling of the nozzle," *Rapid Prototyping J.*, vol. 24, no. 6, pp. 973–987, Aug. 2018.
- [18] R. Comminal, M. P. Serdeczny, D. B. Pedersen, and J. Spangenberg, "Numerical modeling of the strand deposition flow in extrusion-based additive manufacturing," *Additive Manuf.*, vol. 20, pp. 68–76, Mar. 2018.
- [19] P. Foteinopoulos, A. Papacharalampopoulos, and P. Stavropoulos, "On thermal modeling of additive manufacturing processes," *CIRP J. Manuf. Sci. Technol.*, vol. 20, pp. 66–83, Jan. 2018, doi: [10.1016/j.cirpj.2017.09.007](https://doi.org/10.1016/j.cirpj.2017.09.007).
- [20] C. Pannier, M. Wu, D. Hoelzle, and K. Barton, "LPV models for jet-printed heightmap control," in *Proc. Amer. Control Conf. (ACC)*, Jul. 2019, pp. 5402–5407.
- [21] D. Ding, Z. Pan, D. Cuiuri, H. Li, S. van Duin, and N. Larkin, "Bead modelling and implementation of adaptive MAT path in wire and arc additive manufacturing," *Robot. Comput.-Integr. Manuf.*, vol. 39, pp. 32–42, Jun. 2016, doi: [10.1016/j.rcim.2015.12.004](https://doi.org/10.1016/j.rcim.2015.12.004).
- [22] A. Herali , A.-K. Christiansson, and B. Lennartson, "Height control of laser metal-wire deposition based on iterative learning control and 3D scanning," *Opt. Lasers Eng.*, vol. 50, no. 9, pp. 1230–1241, Sep. 2012.
- [23] J. Xiong, Z. Yin, and W. Zhang, "Closed-loop control of variable layer width for thin-walled parts in wire and arc additive manufacturing," *J. Mater. Process. Technol.*, vol. 233, pp. 100–106, Jul. 2016, doi: [10.1016/j.jmatprotec.2016.02.021](https://doi.org/10.1016/j.jmatprotec.2016.02.021).
- [24] G. Tapia and A. Elwany, "A review on process monitoring and control in metal-based additive manufacturing," *J. Manuf. Sci. Eng.*, vol. 136, no. 6, Dec. 2014, Art. no. 060801.
- [25] B. Altun and K. Barton, "Exponential stability of nonlinear differential repetitive processes with applications to iterative learning control," *Automatica*, vol. 81, pp. 369–376, Jul. 2017, doi: [10.1016/j.automatica.2017.04.004](https://doi.org/10.1016/j.automatica.2017.04.004).
- [26] H. K. Khalil, *Nonlinear Systems*, 3rd ed. Upper Saddle River, NJ, USA: Prentice-Hall, 2002.
- [27] J. J. Koliha and I. Stra kraba, "Power bounded and exponentially bounded matrices," *Appl. Math.*, vol. 44, no. 4, pp. 289–308, Aug. 1999.
- [28] R. A. Horn and C. R. Johnson, *Matrix Analysis*. Cambridge, U.K.: Cambridge Univ. Press, 2012.
- [29] D. Aksoy, E. C. Balta, D. M. Tilbury, and K. Barton, "A control-oriented model for bead cross-sectional geometry in fused deposition modeling," in *Proc. Amer. Control Conf. (ACC)*, Jul. 2020, pp. 474–480.
- [30] D. Ahn, J.-H. Kweon, S. Kwon, J. Song, and S. Lee, "Representation of surface roughness in fused deposition modeling," *J. Mater. Process. Technol.*, vol. 209, nos. 15–16, pp. 5593–5600, Aug. 2009.
- [31] H. Zomorodi and R. G. Landers, "Extrusion based additive manufacturing using explicit model predictive control," in *Proc. Amer. Control Conf. (ACC)*, Jul. 2016, pp. 1747–1752.
- [32] Z. Wang, P. M. Sammons, C. P. Pannier, K. Barton, and D. J. Hoelzle, "System identification of a discrete repetitive process model for electrohydrodynamic jet printing," in *Proc. Annu. Amer. Control Conf. (ACC)*, Jun. 2018, pp. 4464–4471.
- [33] P. Hagqvist, A. Herali , A.-K. Christiansson, and B. Lennartson, "Resistance based iterative learning control of additive manufacturing with wire," *Mechatronics*, vol. 31, pp. 116–123, Oct. 2015.
- [34] L. Lu, J. Zheng, and S. Mishra, "A layer-to-layer model and feedback control of ink-jet 3-D printing," *IEEE/ASME Trans. Mechatronics*, vol. 20, no. 3, pp. 1056–1068, Jun. 2015.
- [35] B. N. Turner, R. Strong, and S. A. Gold, "A review of melt extrusion additive manufacturing processes: I. Process design and modeling," *Rapid Prototyping J.*, vol. 20, no. 3, pp. 192–204, Apr. 2014.
- [36] Y. Guo and S. Mishra, "A predictive control algorithm for layer-to-layer ink-jet 3D printing," in *Proc. Amer. Control Conf. (ACC)*, Jul. 2016, pp. 833–838.
- [37] M. S. Branicky, "Multiple Lyapunov functions and other analysis tools for switched and hybrid systems," *IEEE Trans. Autom. Control*, vol. 43, no. 4, pp. 475–482, Apr. 1998.
- [38] G.-C. Rota and G. Strang, "A note on the joint spectral radius," *Indagatione Math.*, vol. 22, pp. 379–381, Apr. 1960.
- [39] D. J. Hartfiel, *Nonhomogeneous Matrix Products*. Singapore: World Scientific, 2002.



Efe C. Balta (Graduate Student Member, IEEE) received the B.S. degree in manufacturing engineering from the Faculty of Mechanical Engineering, Istanbul Technical University, Istanbul, Turkey, in 2016, and the M.S. degree in mechanical engineering from the University of Michigan, Ann Arbor, MI, USA, in 2018, where he is currently pursuing the Ph.D. degree in mechanical engineering.

His research interests include control theory and applications, manufacturing science, additive manufacturing, robotics, optimization, and systems engineering.



Dawn M. Tilbury (Fellow, IEEE) received the B.S. degree (*summa cum laude*) in electrical engineering from the University of Minnesota, Minneapolis, MN, USA, in 1989, and the M.S. and Ph.D. degrees in electrical engineering and computer sciences from the University of California at Berkeley, Berkeley, CA, USA, in 1992 and 1994, respectively.

In 1995, she joined the Mechanical Engineering Department, University of Michigan, Ann Arbor, MI, USA, where she is currently a Professor, with a joint appointment as a Professor of EECS.

In June of 2017, she became the Assistant Director for Engineering at the National Science Foundation while maintaining her position at the University of Michigan. She has published more than 150 articles in refereed journals and conference proceedings. Her research interest includes control systems, including applications to robotics and manufacturing systems.



Kira Barton (Member, IEEE) received the B.Sc. degree in mechanical engineering from the University of Colorado at Boulder, Boulder, CO, USA, in 2001, and the M.Sc. and Ph.D. degrees in mechanical engineering from the University of Illinois at Urbana-Champaign, Champaign, IL, USA, in 2006 and 2010, respectively.

She held a post-doctoral research position at the University of Illinois from Fall 2010 until Fall 2011, at which point she joined the Mechanical Engineering Department, University of Michigan, Ann Arbor, MI, USA. She is currently an Associate Professor and a Miller Faculty Scholar with the Department of Mechanical Engineering, University of Michigan. She conducts research in modeling, sensing, and control for applications in advanced manufacturing and robotics, with a specialization in cooperative learning and smart manufacturing.

Dr. Barton was a recipient of the NSF CAREER Award in 2014, the 2015 SME Outstanding Young Manufacturing Engineer Award, the 2015 University of Illinois, Department of Mechanical Science and Engineering Outstanding Young Alumni Award, the 2016 University of Michigan, Department of Mechanical Engineering Department Achievement Award, and the 2017 ASME Dynamic Systems and Control Young Investigator Award.